Biomechanics and Modeling in Mechanobiology (2019) 18:1005–1030
https://doi.org/10.1007/s10237-019-01126-4

ORIGINAL PAPER

A CFD-based Kriging surrogate modeling approach for predicting device-specific hemolysis power law coefficients in blood-contacting medical devices

Brent A. Craven[1] · Kenneth I. Aycock[1] · Luke H. Herbertson[1] · Richard A. Malinauskas[1]

Received: 1 June 2018 / Accepted: 9 February 2019 / Published online: 27 February 2019

Abstract
Most stress-based hemolysis models used in computational fluid dynamics (CFD) are based on an empirical power law correlation between hemolysis generation and the flow-induced stress and exposure time. Empirical model coefficients are typically determined by fitting global hemolysis measurements in simplified blood shearing devices under uniform shear conditions and with well-defined exposure times. CFD simulations using these idealized global empirical coefficients are then performed to predict hemolysis in a medical device with complex hemodynamics. The applicability, however, of this traditional approach of using idealized coefficients for a real device with varying exposure times and non-uniform shear is currently unknown. In this study, we propose a new approach for determining device- and species-specific hemolysis power law coefficients (C, a, and b). The approach consists of calculating multiple hemolysis solutions using different sets of coefficients to map the hemolysis response field in three-dimensional (C, a, b) parameter space. The resultant response field is then compared with experimental data in the same device to determine the coefficients that when incorporated into the locally defined power law model yield correct global hemolysis predictions. We first develop the generalized approach by deriving analytical solutions for simple uniform and non-uniform shear flows (planar Couette flow and circular Poiseuille flow, respectively) that allow us to continuously map the hemolysis solution in (C, a, b) parameter space. We then extend our approach to more practical cases relevant to blood-contacting medical devices by replacing the requirement for an analytical solution in our generalized approach with CFD and Kriging surrogate modeling. Finally, we apply our verified CFD-based Kriging surrogate modeling approach to predict the device- and species-specific power law coefficients for developing laminar flow in a small capillary tube. We show that the resultant coefficients are much different than traditional idealized coefficients obtained from simplified uniform shear experiments and that using such idealized coefficients yields a highly inaccurate prediction of hemolysis that is in error by more than 2000% compared to experiments. Our approach and surrogate modeling framework may be applied to more complex medical devices and readily extended to determine empirical coefficients for other continuum-based models of hemolysis and other forms of flow-induced blood damage (e.g., platelet activation and thrombosis).

Keywords Hemolysis · Blood damage · Power law model · Kriging surrogate modeling

1 Introduction

Flow-induced damage to red blood cells (RBCs) and the subsequent release of hemoglobin, termed mechanical hemolysis, can be detrimental in a variety of blood-contacting medical devices (e.g., blood pumps and heart valves). The fluid dynamics of mechanical hemolysis has been studied since the 1960s (Kusserow and Kendall 1963; Blackshear et al. 1965, 1966), and since then, it has become widely accepted that hemolysis is primarily a function of the magnitude of

✉ Brent A. Craven
brent.craven@fda.hhs.gov

[1] Division of Applied Mechanics, Office of Science and Engineering Laboratories, Center for Devices and Radiological Health, United States Food and Drug Administration, Silver Spring, MD, USA

flow-induced stress that RBCs are exposed to and the time duration of exposure.

Traditionally, in vitro experiments are performed to quantify the hemolytic potential of a blood-contacting medical device. Over the past several decades, however, computational fluid dynamics (CFD) has become more widely adopted and used to predict hemolysis potential (e.g., Bludszuweit 1995; Pinotti and Rosa 1995; Apel et al. 2001; Song et al. 2003; Goubergrits and Affeld 2004; Fraser et al. 2012; Goubergrits et al. 2016). Currently, CFD is capable of predicting relative levels of hemolysis in medical devices, which is valuable for comparative purposes (e.g., design optimization, evaluating the influence of minor changes to an existing device). But, reliably predicting *absolute* hemolysis levels compared to experiments has proved to be much more challenging (e.g., see Taskin et al. 2012; Yu et al. 2017). Consequently, CFD cannot yet be relied upon to accurately predict the true hemolytic potential and, thus, the safety of medical devices in regulatory evaluations (Malinauskas et al. 2017).

There are two common approaches to numerically model flow-induced mechanical hemolysis: strain-based models (Arora et al. 2004; Chen and Sharp 2010; Vitale et al. 2014; Ezzeldin et al. 2015; Sohrabi and Liu 2017; Toninato et al. 2017) and stress-based power law models (Grigioni et al. 2005; Fraser et al. 2012; Taskin et al. 2012; Hariharan et al. 2015; Heck et al. 2017). Most strain-based models use a multi-scale approach to predict the strain that individual RBCs undergo in response to spatial and temporal gradients in the surrounding flow field. The blood cells in strain-based models are resolved at varying levels of fidelity, ranging from RBCs being approximated as deforming ellipsoidal droplets (Arora et al. 2004) to high-fidelity modeling of RBC fluid–structure interaction using a coarse-grained particle dynamics approach (Ezzeldin et al. 2015). Recent strain-based multi-scale modeling by Sohrabi and Liu (2017) has even extended this approach to the molecular scale to predict hemoglobin released from deformable RBCs due to either rupture of the cell membrane at large strains or the formation of nanopores in a stretched RBC membrane and the subsequent escape of hemoglobin molecules (termed sublethal or sublytic hemolysis) at smaller strains. Though such multi-scale models have the future potential to accurately predict absolute hemolysis levels for an entire device from first principles, due to their computational expense high-fidelity multi-scale approaches are presently restricted to modeling a small number of RBCs. Additionally, more accurate predictions of RBC damage from first principles using such multi-scale approaches await a more firm theoretical and experimental underpinning of some of the underlying cellular and molecular biophysics, particularly with regard to sublytic hemolysis (e.g., see Ezzeldin et al. 2015; Sohrabi and Liu 2017).

In contrast, stress-based power law models utilize a continuum approach that relies on the empirical correlation first proposed by Giersiepen et al. (1990) that relates plasma free hemoglobin generation to the shear stress magnitude (σ_{shear}) in Pascals and exposure time (t_{exp}) in seconds:

$$H = \frac{\left(1 - H_{\text{ct}}/100\right) fHb}{Hb} = C\, t_{\text{exp}}^{a}\, \sigma_{\text{shear}}^{b}. \tag{1}$$

Here, H is the relative fraction of plasma free hemoglobin to the total blood hemoglobin (which is comprised of both free hemoglobin in the plasma and hemoglobin that remains within intact RBCs), H_{ct} is the percent hematocrit, *fHb* is the plasma free hemoglobin concentration (mg/dl plasma), *Hb* is the total blood hemoglobin concentration (mg/dl blood), and C, a, and b are empirical coefficients. Note that the multiplier $(1 - H_{\text{ct}}/100)$ is required to accommodate the differing definitions of *fHb* and *Hb*, which are defined in terms of plasma volume and total blood volume, respectively. The dimensionless empirical coefficients a and b and the dimensional coefficient C (with units of $\text{Pa}^{-1}\text{s}^{-1}$) are typically determined from measurements of hemolysis in Couette-type shearing devices under uniform shear conditions (e.g., see Heuser and Opitz 1980; Zhang et al. 2011; Ding et al. 2015 and Table 1).

Historically, continuum-based power law models have been the most popular approach to predicting mechanical hemolysis using CFD as they are readily incorporated into existing CFD software using either an Eulerian or Lagrangian formulation at the macroscale. However, there are several major challenges with using power law models to accurately predict absolute hemolysis levels that have yet to be fully addressed. At their core, most power law models recast the global empirical correlation of Eq. 1 to a form such that it is applied locally at either every point along

Table 1 Global empirical power law coefficients for $H = C\, t_{\text{exp}}^{a}\, \sigma_{\text{shear}}^{b}$ developed from experiments acquired in Couette-type shearing devices with laminar flow, uniform shear conditions, and with well-defined exposure times

Refs.	Animal Species	C	a	b
Giersiepen et al. (1990)	Human	3.62×10^{-7}	0.785	2.416
Song et al. (2003)/ Heuser and Opitz (1980)[a]	Porcine	1.8×10^{-8}	0.765	1.991
Zhang et al. (2011)[b]	Ovine	1.228×10^{-7}	0.6606	1.9918
Ding et al. (2015)	Human	3.458×10^{-8}	0.2777	2.0639
Ding et al. (2015)	Porcine	6.701×10^{-6}	0.2778	1.0981
Ding et al. (2015)[b]	Ovine	1.228×10^{-7}	0.6606	1.9918
Ding et al. (2015)	Bovine	9.772×10^{-7}	0.2076	1.4445

[a]Developed by Song et al. (2003) using the experimental data of Heuser and Opitz (1980)

[b]Coefficients derived from the same experimental data

a streamline (for Lagrangian methods) or at every point in the flow domain of the device (for Eulerian methods). These local power law formulations still require the empirical coefficients C, a, and b, and, in the absence of more appropriate values, investigators typically use power law coefficients originally obtained by fitting the global correlation of Eq. 1 using hemolysis data acquired in laminar Couette flow shearing devices under uniform shear conditions and with well-defined exposure times (Table 1). Computational simulations are then performed to predict the hemolytic potential of a medical device, such as a blood pump, with a complex hemodynamic flow field that often includes turbulence, highly non-uniform stress (both extensional and shear), and where there are not well-defined stress exposure times. This traditional approach to predicting hemolysis in blood-contacting medical devices using CFD and continuum-based power law models is illustrated in Fig. 1a.

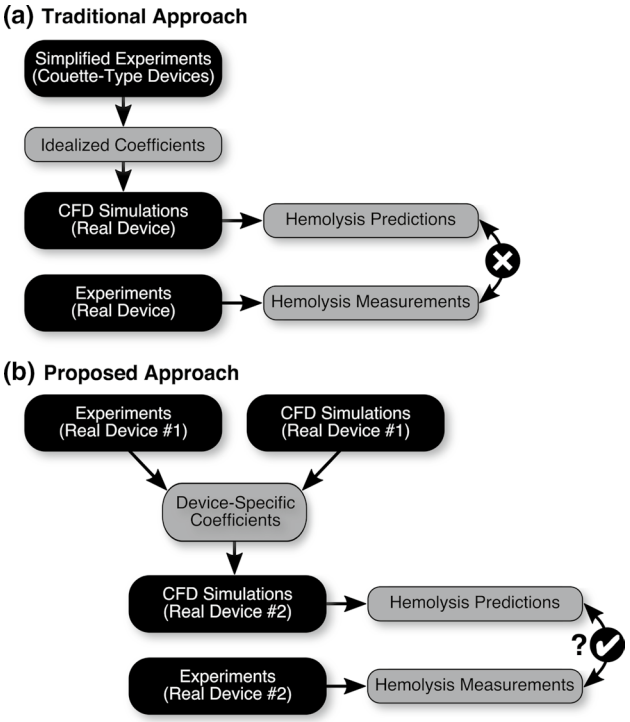

Fig. 1 **a** Traditional and **b** proposed approach for predicting the hemolytic potential of a blood-contacting medical device using CFD and continuum-based power law models. In the traditional approach (**a**), global empirical power law coefficients obtained from simplified experiments (Table 1) are used to predict hemolysis in medical devices with extremely complex flow conditions. In the proposed approach (**b**), device-specific power law coefficients are obtained by combining experimental hemolysis measurements and CFD simulations (see the main text for details). Theoretically, these device-specific coefficients may then be applied to predict the hemolytic potential of the same device at different operating conditions, or perhaps even similar devices, denoted here as *Real Device #2*

The applicability, however, of using global power law coefficients derived from simplified experiments to predict the spatial distribution of hemolysis production based on local values of stress in a medical device with extremely complex flow conditions is currently unknown. The wide range of power law coefficients reported in the literature from experiments in Couette-type devices with similar uniform shear conditions (Table 1) seems to indicate that coefficients may be device-specific, even for simplified devices. Indeed, the existence of device-specific power law coefficients may be one of the main reasons why it is so challenging to predict absolute hemolysis levels in medical devices using coefficients from simplified experiments (e.g., see Taskin et al. 2012; Yu et al. 2017). To further complicate matters, hemolysis power law coefficients also depend on the species of animal blood used in experiments (Ding et al. 2015; see Table 1).

In application, if hemolysis power law coefficients are device- and species-specific, it is currently unclear how to best determine reliable coefficients for a specific device and for a specific species of animal blood. As concluded by Yu et al. (2017), who found that using different sets of coefficients from the literature yields hemolysis predictions in a rotary blood pump that vary by up to a factor of 50, establishing more reliable hemolysis power law coefficients is "essential to increase prediction accuracy." The challenge is that, in medical devices with complex flow fields and highly non-uniform stress, a global power law is difficult to define because of the ambiguity of defining a characteristic stress and exposure time. Rather, in such practical applications the power law must be defined and applied in a local fashion, in which case the power law coefficients represent values that yield correct global hemolysis predictions when the power law is applied locally.

Here, we propose a new approach for determining device- and species-specific hemolysis power law coefficients that is conceptually illustrated in Fig. 1b. The approach requires: (i) quantification of the entire flow field in the device and (ii) hemolysis measurements. Given detailed quantification of the velocity field from CFD (or from whole-field velocity measurements—e.g., via volumetric particle image velocimetry), the stress field may be calculated and the power law applied locally to determine the coefficients that yield global hemolysis predictions that match the hemolysis measurements. Theoretically, the resultant device- and species-specific power law coefficients can then be applied in the same device to predict hemolysis at different operating conditions, or perhaps even in similar devices. In either case, compared with the traditional approach of using local power law formulations with global empirical coefficients derived from simplified experiments (Fig. 1a), this approach offers the hope of more accurately predicting hemolysis levels in blood-contacting medical devices—at least until

more advanced physics-based models are developed that are capable of accurately predicting absolute hemolysis levels in a device.

2 Objectives

The objectives of this study are to:

1. Develop a novel approach for determining device- and species-specific hemolysis power law coefficients. We choose a specific form of the hemolysis power law model that permits the derivation of analytical solutions for simplified cases (planar Couette flow and circular Poiseuille flow), allowing us to develop and verify our generalized methodology using analytical methods. We then extend our generalized approach to more practical cases relevant to blood-contacting medical devices wherein analytical solutions are unavailable. Here, we replace the requirement for an analytical solution in our generalized approach with CFD and a numerical method known as surrogate modeling, which we also verify by comparing with the results obtained using exact analytical solutions.
2. Apply our verified CFD and surrogate modeling approach to investigate the applicability of the traditional approach of using global empirical coefficients obtained from simplified experiments to predict hemolysis in a device with highly non-uniform stress. Here, we strategically choose a case (developing laminar flow in a capillary tube) with appreciable non-uniform stress due to laminar flow in a relatively simple geometry. Importantly, this allows us to have a high degree of confidence in our CFD simulations and to avoid the complications of turbulence modeling and the uncertainties associated with the influence of turbulence on hemolysis. Given available experimental data in this capillary tube geometry, using our CFD and surrogate modeling approach we predict the device- and species-specific hemolysis power law coefficients for this case and compare them with traditional empirical coefficients obtained from simplified experiments (Table 1). We also show the error incurred by using traditional power law coefficients to predict hemolysis in this device using CFD.

3 Materials and methods

3.1 Governing equations

In this study, we consider the laminar, incompressible flow of blood that is treated as a Newtonian fluid. Though blood is viscoelastic and shear-thinning, it behaves as a Newtonian fluid when the shear rate is above approximately $100\,\mathrm{s}^{-1}$ (Aycock et al. 2016), as it is in most regions of the cases considered in the present study. Under these conditions, the flow is governed by the incompressible continuity

$$\nabla \cdot \mathbf{u} = 0 \tag{2}$$

and Navier–Stokes equations

$$\frac{\partial \mathbf{u}}{\partial t} + (\mathbf{u} \cdot \nabla)\mathbf{u} = -\frac{\nabla p}{\rho} + \nu \nabla^2 \mathbf{u} \tag{3}$$

where $\mathbf{u}$ is the velocity vector, p is pressure, ρ is density, and ν is the kinematic viscosity.

For hemolysis, we use the Eulerian power law model. The advantage of this specific hemolysis model for the present study is that analytical solutions can be derived for simplified cases (e.g., see Hariharan et al. 2015), allowing us to develop and verify our generalized methodology for predicting device-specific coefficients. The analytical solutions are also valuable for verifying results from numerical modeling and simulation.

Following the approach of others (Garon and Farinas 2004; Trias et al. 2014; Yu et al. 2017), the Eulerian power law model can be derived beginning with Eq. 1. The power law relationship is first rewritten as

$$H' = H^{1/a} = \left(C\,\sigma^b\right)^{1/a} t \tag{4}$$

where H' is a linearized plasma free hemoglobin fraction defined for mathematical convenience to linearize Eq. 1 with respect to time. This form of the hemolysis power law can be temporally differentiated and cast to an Eulerian reference frame, yielding a partial differential equation for the production and transport of H':

$$\frac{\partial H'}{\partial t} + (\mathbf{u} \cdot \nabla)H' = \left(C\,\sigma^b\right)^{1/a}. \tag{5}$$

The right-hand side of Eq. 5 represents the local production of the linearized plasma free hemoglobin fraction, H', due to flow-induced stress, which can be non-uniform and include non-shear (extensional) stress components—both of which are deviations from the uniform shear conditions used to develop the underlying global empirical power law relationship of Eq. 1 (e.g., see Giersiepen et al. 1990; Zhang et al. 2011; Ding et al. 2015).

3.2 Scalar stress

The Eulerian power law model of Eq. 5 requires a scalar measure, σ, of the flow-induced stress, which is a second-order tensor. For the laminar, incompressible flow of blood considered in this study the flow-induced stress is due to viscous effects. The viscous stress tensor is defined as

$$\boldsymbol{\sigma} = 2\mu\mathbf{S} \tag{6}$$

where μ is the dynamic viscosity and $\mathbf{S}$ is the strain rate tensor:

$$\mathbf{S} = \frac{1}{2}\left(\nabla\mathbf{u} + (\nabla\mathbf{u})^T\right). \tag{7}$$

To quantify the magnitude of the viscous stress tensor, we define an effective scalar stress as:

$$\sigma = \sqrt{\frac{1}{2}\boldsymbol{\sigma} : \boldsymbol{\sigma}}. \tag{8}$$

As recently noted by Faghih and Sharp (2016), Eq. 8 is the most appropriate scalar measure of stress for use in the hemolysis power law model as it yields the fluid shear stress under pure shear conditions. This is especially critical if the power law model is used with empirical coefficients derived from experiments in Couette-type shearing devices under uniform shear conditions, which is traditionally the case (see Fig. 1a and related discussion).

3.3 Hemolysis indices

In "Appendix 1", we provide a thorough introduction to the various hemolysis indices that are used in the present study. Here, we briefly define each of the indices and refer the reader to "Appendix 1" for further details.

For a single-pass experiment, the hemolytic potential of a blood-contacting medical device is typically quantified in terms of a single-pass index of hemolysis defined as:

$$IH_{\text{sp}} = \frac{\left(1 - H_{\text{ct}}/100\right)fHb}{Hb}. \tag{9}$$

Physically, IH_{sp} represents the relative mass fraction of the total blood hemoglobin that is released from the RBCs as blood flows through the device. By definition, IH_{sp} must be between 0 and 1.

For a multi-pass experiment, the hemolytic potential of a device is often quantified in terms of a "modified index of hemolysis" (*MIH*) defined as

$$MIH = 10^6 \frac{\left(1 - H_{\text{ct}}/100\right)fHb}{Hb}\left(\frac{V}{Q\,\Delta t}\right) \tag{10}$$

where V is the total volume of blood in the flow loop, Q is the volumetric flow rate, and Δt is the time duration of the experiment (Mueller et al. 1993). In general, *MIH* physically represents the relative fraction of the total blood hemoglobin that is released from the RBCs per pass through the device. By definition, then, *MIH* must be between 0 and 10^6.

To directly compare with hemolysis experiments, an appropriate index of hemolysis must be calculated from analytical or numerical solutions of flow and hemolysis in a device. As derived in "Appendix 1", given an analytical or numerical solution of flow and hemolysis, we can calculate an effective single-pass index of hemolysis as:

$$IH_{\text{outlet}} = \overline{H}_{\text{outlet}} = \frac{\int_{\text{outlet}} (H\,\mathbf{u}) \cdot \mathrm{d}\mathbf{A}}{\int_{\text{outlet}} \mathbf{u} \cdot \mathrm{d}\mathbf{A}} \tag{11}$$

where the integration is performed over the outlet of the flow domain. This may be directly compared with experimental values of IH_{sp} from single-pass measurements. For multi-pass devices, analytical or numerical predictions of IH_{outlet} may be scaled by 10^6 and directly compared with experimental values of *MIH*.

3.4 Analytical and numerical methods

In general, predictions of the hemolytic potential of a medical device using the Eulerian power law model are obtained following the steps summarized in Algorithm 1. In the rare case that closed-form analytical solutions are available for all steps in Algorithm 1, the governing equations can be solved exactly to predict hemolysis. Importantly, it should be noted, however, that such predictions still depend on the power law coefficients, C, a, and b. But, in general, exact flow and hemolysis solutions are not available in a real device, in which case CFD is used to numerically compute each of the steps in Algorithm 1.

Algorithm 1 Hemolysis prediction in a blood-contacting medical device using the Eulerian power law model.

1. Solve incompressible continuity and Navier-Stokes equations for the pressure, p, and velocity, $\mathbf{u}$, fields (Eqs. 2 and 3)
2. Calculate the viscous stress tensor field, $\boldsymbol{\sigma}$ (Eqs. 6 and 7)
3. Calculate the effective scalar stress field, σ (Eq. 8)
4. Solve for the production and transport of the linearized plasma free hemoglobin fraction, H' (Eq. 5)
5. Calculate the plasma free hemoglobin fraction, H (Eq. 4)
6. Calculate the index of hemolysis at the outlet of the device, IH_{outlet} (Eq. 11)

In the present study, we derive closed-form analytical solutions for hemolysis in two simplified cases: planar Couette flow and circular Poiseuille flow. Given appropriate assumptions in each case, the governing equations are simplified and exact solutions are derived for each step in Algorithm 1. In the final step, the index of hemolysis is calculated by symbolic integration of Eq. 11 using Mathematica (version 11.1).

As a third more general case, we consider hemolysis in the developing laminar flow in a small capillary tube, for which a closed-form analytical solution does not exist. In

this case, CFD is used to numerically solve each step in Algorithm 1. Assuming steady-state conditions, the Semi-Implicit Method for Pressure-Linked Equations (SIMPLE) algorithm is used to numerically solve Eqs. 2 and 3 in OpenFOAM (version 2.4) using second-order accurate spatial discretization schemes. The normalized solution residuals are forced to be less than 10^{-4} to ensure iterative convergence of the steady-state solution. Values of various primitive solution variables (minimum and maximum pressure, maximum velocity) and integrated quantities (outlet flow rate, integrated force) are also monitored throughout the simulation to assess iterative convergence.

Given the flow solution and the resultant stress field (steps 1–3 in Algorithm 1), the production and transport of H' are computed using a custom Eulerian power law hemolysis solver developed in OpenFOAM. Quasi-steady hemolysis solutions are obtained by solving Eq. 5 using second-order accurate spatial discretization schemes and the SLTS stabilized local time-stepping scheme available in OpenFOAM with a local Courant number of 0.1. Quasi-steady convergence of the solution is assessed by monitoring the H' field and the integrated flux of H' at the outlet. Finally, given the steady flow and hemolysis solutions, the index of hemolysis at the outlet, IH_{outlet}, is calculated by numerically integrating Eq. 11 in OpenFOAM.

To ensure correct implementation of the Eulerian power law model in OpenFOAM, a rigorous verification of the hemolysis solver was performed. This included comparing simulation results using a relatively fine mesh with exact analytical solutions of flow and hemolysis for steady, axisymmetric fully developed flow in a small capillary tube (i.e., circular Poiseuille flow). In summary, the comparison showed a maximum percent difference between the CFD and analytical solutions of less than approximately 0.1% for velocity, viscous scalar stress, plasma free hemoglobin fraction, and the index of hemolysis at the outlet of the tube. Given the close correspondence between the CFD and analytical solutions, this confirms that the Eulerian power law model is implemented correctly in OpenFOAM.

3.5 Three-dimensional (*C*, *a*, *b*) parameter space

To determine device- and species-specific hemolysis power law coefficients, given the flow field solution in a device (steps 1–3 in Algorithm 1), the Eulerian power law model can be solved using different combinations of power law coefficients (C, a, b) and the results compared with experimental hemolysis data. As schematically illustrated in Fig. 2, by mapping the hemolysis response field in three-dimensional (C, a, b) parameter space we can identify the power law coefficients that, when incorporated into the Eulerian power law model (Eq. 5), yield hemolysis

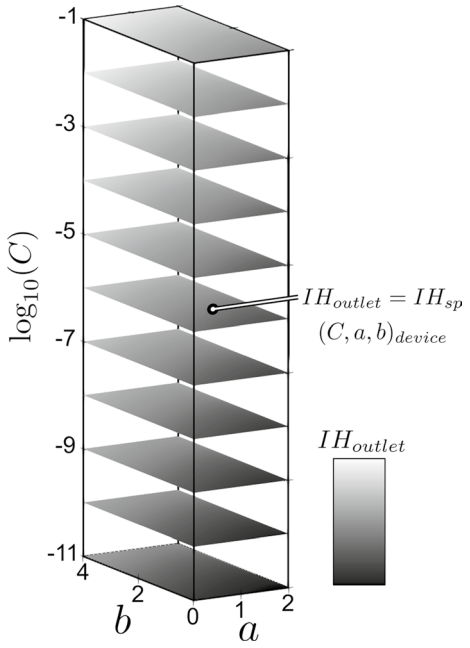

Fig. 2 Schematic illustration of the three-dimensional (C, a, b) parameter space used to determine device- and species-specific hemolysis power law coefficients. Note that the C parameter is log10-transformed for visualization purposes to accommodate the wide range of possible values in contrast to the comparatively narrow range of values expected for the a and b parameters (see Table 1)

predictions of IH_{outlet} (Eq. 11) that match experimental measurements of either IH_{sp} (Eq. 9) or MIH (Eq. 10) from single-pass or multi-pass experiments, respectively. That is, conceptually the device- and species-specific coefficients are determined by mapping all possible solutions of $IH_{\text{outlet}}(C, a, b)$ in three-dimensional parameter space and comparing the results with experimental data to determine what combinations of C, a, and b yield hemolysis predictions that match the experiments.

3.6 Kriging surrogate modeling

In cases where closed-form analytical solutions exist for all steps of Algorithm 1, IH_{outlet} is continuously defined as a function of C, a, and b. Accordingly, all possible hemolysis solutions are easily mapped in three-dimensional (C, a, b) parameter space using the analytical solution. In general, however, this is not the case in a real device, where closed-form analytical solutions do not exist. In such practical cases, all steps of Algorithm 1 must be solved numerically using CFD. Given the computational expense of CFD and the fact that a separate CFD simulation is required to predict hemolysis for each combination of C, a, and b, it is not generally possible to map the entire three-dimensional (C, a, b) parameter space with high fidelity. For this, we use a technique known as Kriging surrogate modeling.

Surrogate modeling (also known as metamodeling or response surface modeling) is a method used to fit or interpolate the results from expensive computer simulations using a comparatively inexpensive surrogate response function that may be leveraged to predict results between simulation data points in the parameter (or design) space of interest (Jones 2001; Forrester et al. 2008). There are two general classes of surrogate models: interpolating and non-interpolating. When used with deterministic computer simulations, interpolation-based surrogate modeling methods are preferred because they interpolate the computer simulation results and are, thus, guaranteed to return the same result as the computer simulation at parameter space locations where simulation data exist. Additionally, interpolation-based methods better capture the shape of complex, multimodal response functions compared to non-interpolating response surface methods that fit a polynomial function to the simulation data (Jones 2001; Forrester et al. 2008).

Surrogate modeling using Kriging interpolation—or Kriging surrogate modeling—is especially powerful because it has a statistical underpinning that provides an estimate of the error in the interpolation, termed the "predictor" (Jones 2001). Given an initial set of simulation data points, a Kriging predictor is constructed that includes an estimate of the error. The estimated error is then used to identify parameter space locations where new simulation data can be added to improve (or update) the predictor in subsequent iterations. In this way, Kriging surrogate modeling can be used to either: (i) obtain a high-fidelity representation of the global parameter space by driving down the maximum predicted error, or (ii) search for a global optimum by exploiting the surrogate to drive down the local error in the vicinity of the predicted optimum location (Jones 2001; Forrester et al. 2008).

In the present study, we developed a Kriging surrogate modeling framework in Python that uses the pyKriging package (Paulson and Ragkousis 2015) to construct a Kriging surrogate of the hemolysis response field in three-dimensional (C, a, b) parameter space from CFD data obtained from simulations performed using OpenFOAM. As illustrated in Algorithm 2, the framework manages the generation of an initial sampling plan, launching CFD simulations, reading the CFD output, constructing the Kriging predictor, generating infill points using either a root mean squared error (RMSE) or expected improvement (EI) criterion (or both), updating the Kriging predictor with new CFD results, searching the predictor for the global optimum, tracking the location of the global optimum, and monitoring convergence of the algorithm. Given the required user input (step 1 in Algorithm 2), the surrogate modeling framework is run in an automated fashion in a parallel computing environment to facilitate the execution of multiple concurrent CFD simulations that can each be run in serial or in parallel.

Algorithm 2 Generalized CFD-based Kriging surrogate modeling framework for predicting device-specific hemolysis power law coefficients. Here we assume the velocity and stress fields (steps 1–3 in Algorithm 1) have been pre-computed.

1. **Input:** (C, a, b) parameter space range and discretization level, number of initial sample points, number of infill points per iteration using root mean squared error (RMSE) and expected improvement (EI) criteria, convergence criteria based on either maximum normalized RMSE or global optimum location (or both), experimental hemolysis data
2. **Initial Sample Points:** Generate a space-filling set of points in (C, a, b) parameter space using Latin hypercube sampling (McKay et al., 1979; Forrester et al., 2008)
3. **Run Hemolysis CFD Simulations:** Given pre-computed velocity and stress field solutions (steps 1–3 in Algorithm 1), run a hemolysis CFD simulation (steps 4–6 in Algorithm 1) for each initial sample point from step 2
4. **Read Hemolysis CFD Results:** Read IH_{outlet} from each hemolysis CFD simulation
5. **Initialize Kriging Predictor:** Construct Kriging predictor using initial hemolysis CFD simulation data from step 4
6. **Evaluate Kriging Predictor in Discrete** (C, a, b) **Parameter Space:** Use initial Kriging predictor to predict IH_{outlet} and the normalized RMSE at all discrete parameter space locations
7. **Iterate:** Iterate to obtain either: (i) an accurate global representation of the IH_{outlet} field in (C, a, b) parameter space, or (ii) the location of the global optimum (i.e., values of C, a, and b that yield a CFD prediction of IH_{outlet} that matches experimental hemolysis measurements of IH_{sp} or MIH)
   (a) **Add Infill Points:** Generate set of infill points using either RMSE or EI criterion from Kriging predictor (or both)
   (b) **Run Hemolysis CFD Simulations:** Compute hemolysis CFD solution for each infill point
   (c) **Read Hemolysis CFD Results:** Read IH_{outlet} for each infill CFD simulation
   (d) **Update Kriging Predictor:** Update predictor with infill CFD simulation results
   (e) **Update RMSE and EI:** Get RMSE and EI from updated Kriging predictor
   (f) **Evaluate Kriging Predictor in Discrete** (C, a, b) **Parameter Space:** Use updated Kriging predictor to predict IH_{outlet} and the normalized RMSE at all discrete parameter space locations
   (g) **If global optimization desired:**
      i. **Calculate objective function:** $J(C, a, b) = |IH_{outlet}(C, a, b) - IH_{sp}|$ for single-pass device or $J(C, a, b) = |10^6 IH_{outlet}(C, a, b) - MIH|$ for multi-pass device
      ii. **Locate global optimum:** Find parameter values $(C, a, b)_{opt}$ at the global minimum of the objective function
   (h) **Check Convergence:**
   If globally accurate surrogate desired: Compare magnitude and iterative behavior of maximum normalized RMSE with input convergence criteria
   If global optimum desired: Compare iterative behavior of $(C, a, b)_{opt}$ and maximum normalized RMSE with input convergence criteria—e.g., $(C, a, b)_{opt}$ unchanged over three successive iterations and maximum normalized RMSE below a specified threshold

The present Kriging surrogate modeling framework may be used to either: (i) obtain an accurate global representation of the hemolysis response field for parameter space exploration and comparison with experimental data, or (ii) find the global optimum, corresponding to the parameter space location $(C, a, b)_{\text{opt}}$ that yields a unique numerical prediction that matches experimental data. The choice depends on the specific application and the behavior of the hemolysis response field—in particular, whether a unique global optimum exists.

4 Results

This section is organized as follows:

- In Sect. 4.1 (Analytical: planar Couette flow), we develop a novel approach for determining device- and species-specific hemolysis power law coefficients. We consider hemolysis in a uniform shear flow (fully developed boundary-driven channel flow; Fig. 3a), a case for which an analytical solution exists for the Eulerian power law model. We first investigate the behavior of the hemolysis response field, IH_{outlet}, in (C, a, b) parameter space and then compare with the hemolysis experiments of Ding et al. (2015) in developing a generalized approach for determining device- and species-specific coefficients.
- In Sect. 4.2 (Analytical: circular Poiseuille flow), we investigate the behavior of the hemolysis response field for a non-uniform shear flow (fully developed pipe flow; Fig. 3b) using exact analytical solutions. Here, we extend our generalized approach for determining device-specific coefficients to more practical cases with non-uniform flow-induced stress, where a global empirical power law is more difficult to define due to the lack of a single characteristic value of shear stress with a corresponding exposure time.
- In Sect. 4.3 (Numerical: device-specific coefficients for developing flow in a small capillary tube), we replace the requirement for an analytical solution in our generalized approach with CFD and Kriging surrogate modeling. After rigorously verifying our CFD-based Kriging surrogate modeling approach (in "Appendix 3"), we apply it in Sect. 4.3 to investigate the applicability of the traditional approach of using global empirical coefficients obtained from simplified experiments to predict hemolysis in a device with highly non-uniform stress. Here, we strategically choose developing laminar flow in a capillary tube (Fig. 3c), a case with appreciable non-uniform stress due to laminar flow in a relatively simple geometry. This allows us to have a high degree of confidence in our CFD simulations and to avoid the complications of turbulence modeling and the uncertainties associated with the influence of turbulence on hemolysis. We first perform a mesh refinement study to ensure the accuracy of our CFD simulations (with details provided in "Appendix 4"). We then combine our CFD-based Kriging surrogate model predictions with the experimental data of Kameneva et al. (2004) to determine the device- and species-specific hemolysis power law coefficients. These coefficients are compared with traditional coefficients derived from Couette-type devices under uniform shear conditions (Table 1), and the accuracy of hemolysis predictions using such traditional idealized coefficients is assessed.

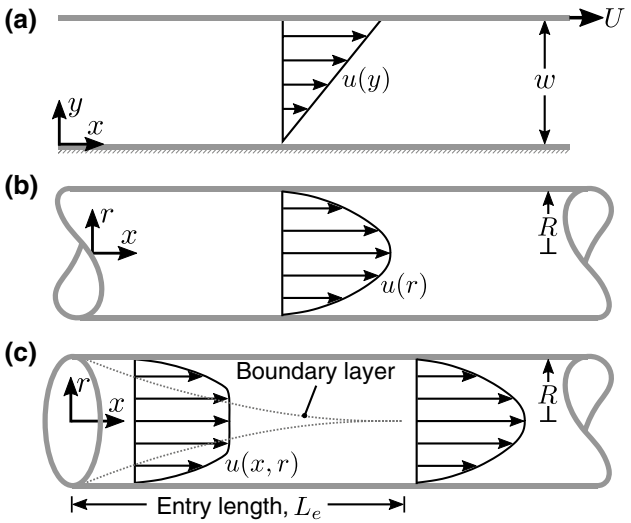

Fig. 3 Schematic illustration of the benchmark cases considered in the present study that include **a** planar Couette flow (fully developed boundary-driven channel flow), **b** circular Poiseuille flow (fully developed pipe flow), and **c** developing laminar flow in a small capillary tube

4.1 Analytical: planar Couette flow

4.1.1 Analytical solution

Assuming steady-state, two-dimensional fully developed flow with no-slip conditions at the boundaries, the classical planar Couette solution for the velocity distribution in the channel is:

$$u(y) = \frac{Uy}{w} \tag{12}$$

where U is the speed of the upper boundary and w is the channel gap width (see Fig. 3a). This linear velocity profile yields a constant viscous scalar stress, calculated from Eqs. 6–8 as:

$$\sigma = \left| \frac{\mu U}{w} \right| \tag{13}$$

where μ is the dynamic viscosity. Given the velocity and stress distributions in the channel and assuming an inlet plasma free hemoglobin fraction of zero ($H(x = 0, y) = 0$), the analytical solution of the Eulerian power law model (Eq. 5) is:

$$H(x, y) = C\,\sigma^b \left(\frac{x}{u(y)}\right)^a = C \left|\frac{\mu U}{w}\right|^b \left(\frac{wx}{Uy}\right)^a \tag{14}$$

where x is the distance from the inlet in the x-coordinate direction. Finally, the index of hemolysis at the channel outlet, IH_{outlet}, is calculated as the integrated flux of $H(x, y)$ at the outlet, located at $x = L$, normalized by the integrated outlet flow rate (Eq. 11), yielding a closed-form analytical solution

$$\begin{aligned} IH_{\text{outlet}} &= \frac{\int_{\text{outlet}} (H\,\mathbf{u}) \cdot \mathrm{d}\mathbf{A}}{\int_{\text{outlet}} \mathbf{u} \cdot \mathrm{d}\mathbf{A}} \\ &= \left.\frac{2C\left(\frac{L}{U}\right)^a \left(\frac{\mu U}{w}\right)^b}{2 - a}\right|_{a<2} \end{aligned} \tag{15}$$

that is confined to a restricted domain in (C, a, b) parameter space with $a < 2$. Here, we assume that $C, a, b, L, w, \mu, U_{\text{avg}} \in \mathbb{R}$ and $L, w, \mu, U_{\text{avg}} > 0$.

4.1.2 Behavior of hemolysis solution

Given the analytical expression in Eq. 15, we can map the IH_{outlet} response field from the Eulerian power law model in three-dimensional (C, a, b) parameter space. To determine the power law coefficients that yield global hemolysis predictions of IH_{outlet} that match experimental measurements, here we use the experimental correlation of Ding et al. (2015) for IH_{sp} (see Table 1) from measurements using bovine blood in a Couette-type shearing device with similar uniform shear conditions as in the present planar Couette flow case. That is, at a specific operating condition characterized by specific values of shear stress and exposure time, we use the analytical solution of Eq. 15 to map IH_{outlet} as a function of C, a, and b. We next extract the value of IH_{outlet} in (C, a, b) parameter space that matches the experimental hemolysis value from the Ding et al. (2015) correlation for bovine blood at the same condition. The device- and species-specific power law coefficients are then determined by identifying the location in (C, a, b) parameter space where IH_{outlet} matches the experimental hemolysis value (see Sect. 3.5 for further discussion).

As shown in Fig. 4a, at a single operating condition ($\sigma = 300\,\text{Pa}, t_{\text{exp}} = 0.25\,\text{s}$) the extracted values of IH_{outlet} that match experimental hemolysis data ($IH_{\text{outlet}} = 0.00277$) form a continuous isosurface that sweeps through the (C,

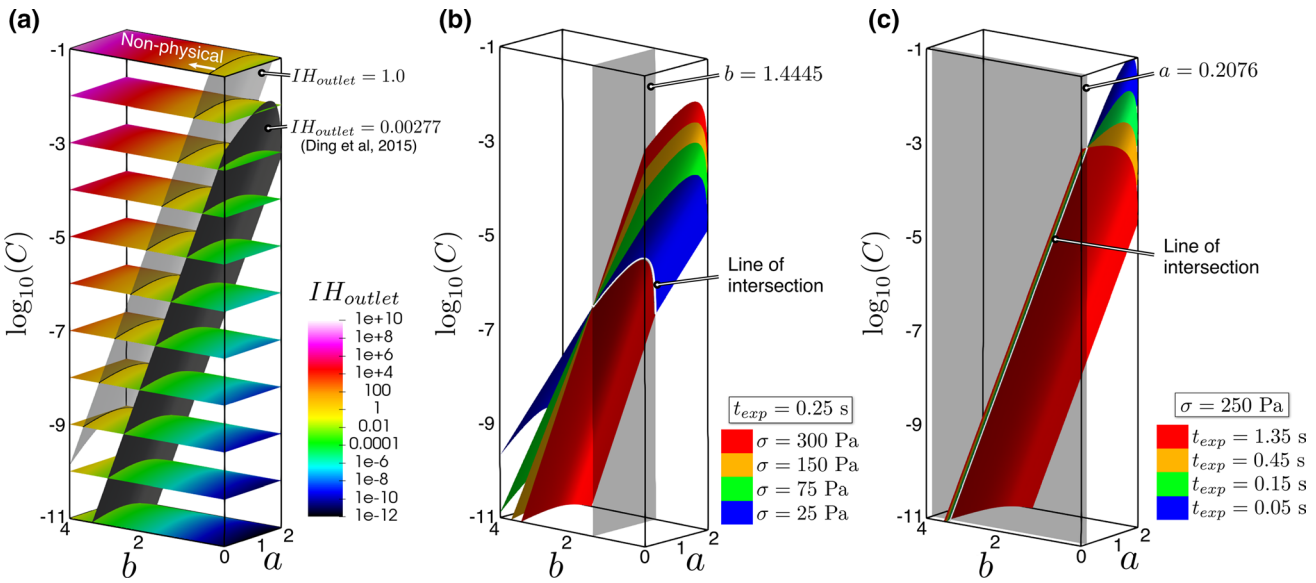

Fig. 4 Map of the index of hemolysis at the outlet, IH_{outlet}, in three-dimensional (C, a, b) parameter space for planar Couette flow (fully developed boundary-driven channel flow). **a** IH_{outlet} response field for a single operating condition ($\sigma = 300\,\text{Pa}, t_{\text{exp}} = 0.25\,\text{s}$). An isosurface of $IH_{\text{outlet}} = 1.0$ is shown as the delineation between physical ($IH_{\text{outlet}} \leq 1.0$) and non-physical ($IH_{\text{outlet}} > 1.0$) hemolysis solutions. An isosurface of $IH_{\text{outlet}} = 0.00277$ is also shown, extracted from the IH_{outlet} response field at a value corresponding to the value calculated from the experimental correlation of Ding et al. (2015) for IH_{sp} in a Couette-type shearing device under the same conditions using bovine blood (see Table 1). **b** Variation in the extracted experimental isosurface with variable shear stress ($\sigma = 25 - 300\,\text{Pa}$) and a constant exposure time ($t_{\text{exp}} = 0.25\,\text{s}$). **c** Variation in the extracted experimental isosurface with variable exposure time ($t_{\text{exp}} = 0.05 - 1.35\,\text{s}$) and a constant shear stress ($\sigma = 250\,\text{Pa}$)

a, b) parameter space. This is especially significant for two reasons. First, it means that in a Couette shearing device, at a single operating condition, there are an infinite number of combinations of power law coefficients that yield the same hemolysis solution defined along a common isosurface. All Eulerian power law model solutions for IH_{outlet} that lie along this isosurface match experimental hemolysis data. This leads us to the second important point: Because there is not a unique combination of C, a, and b that yields a hemolysis prediction that matches experiments at a single condition (i.e., a unique global optimum), standard optimization techniques cannot be utilized to obtain device-specific power law coefficients by minimizing an objective function at a single operating condition (see Algorithm 2 and related discussion). As mentioned in Sect. 3.6, this directly affects our Kriging surrogate modeling strategy, which will be later addressed in Sect. 4.3.

Considering the behavior of the hemolysis solution at a single condition, we note that for large values of C and b the present form of the Eulerian power law model (Eq. 5) can yield highly non-physical hemolysis solutions ($IH_{\text{outlet}} \gg 1.0$). From Fig. 4a, we see that the IH_{outlet} solution varies smoothly from a value approaching zero as C and b approach zero, to extremely large, non-physical values ($IH_{\text{outlet}} \sim 1 \times 10^{10}$) at the opposite corner of the (C, a, b) parameter space domain. From the definitions of H and IH_{outlet} (Eqs. 1 and 11, respectively), the plasma free hemoglobin concentration cannot exceed the total blood hemoglobin concentration, H_b. Thus, IH_{outlet} cannot be greater than unity. This delineation between physical and non-physical solutions is visualized as an isosurface of $IH_{\text{outlet}} = 1$ in Fig. 4a, which illustrates the extent of non-physical solutions that are possible using the current form of the Eulerian power law model.

To characterize how the hemolysis solution varies over multiple conditions, we extract experimental isosurfaces (i.e., isosurfaces extracted from the IH_{outlet} response field that correspond to values calculated from the empirical correlation of Ding et al. (2015) for bovine blood) over a range of conditions by systematically varying shear stress and exposure time. As shown in Fig. 4b, as the magnitude of the shear stress varies at a fixed exposure time, the experimental isosurfaces rotate about a line of intersection that lies in a plane corresponding to $b = 1.4445$, which is equal to the value of the b parameter from the Ding et al. (2015) correlation. That is, when we fix the exposure time and vary the shear stress, a single unique value of the b parameter ($b = 1.4445$) exists that, when used in the Eulerian power law model (Eq. 5), yields hemolysis predictions that match experiments at all conditions. This unique value of b is equal to the value of the b parameter from the experimental correlation of Ding et al. (2015) for bovine blood (Table 1) that was used to obtain the experimental hemolysis data. Similarly, from Fig. 4c we see that as the exposure time varies at a fixed shear stress, the experimental isosurfaces rotate about a line of intersection that lies in a plane corresponding to $a = 0.2076$, which is equal to the value of the a parameter in the Ding et al. (2015) correlation used to calculate the experimental hemolysis values. In each case, this behavior stems from the mathematical form of the power law (Eq. 1), wherein the shear stress (σ_{shear}) is raised to the power of b and exposure time (t_{exp}) is raised to the power of a.

4.1.3 Generalized approach for determining device-specific coefficients

In theory, it is not all that surprising here that, when we extract isosurfaces of IH_{outlet} from Eulerian power law model solutions that match experimental hemolysis values, we recover the power law coefficients of the empirical correlation that was used to obtain the experimental values. Admittedly,—in the present case this is of little value; if we know the power law coefficients in the Couette shearing device from an experimental correlation there is no need to use the Eulerian hemolysis model to calculate them. In general, however, global power law correlations do not exist for real medical devices with complex hemodynamic flow conditions due to the lack of a well-defined characteristic shear stress and exposure time in the device (see Sect. 1 for related discussion). Thus, the significance of the present results for planar Couette flow is that they demonstrate a methodology for calculating device-specific power law coefficients that may be extended to real devices, where a global power law correlation does not exist.

From this perspective, these results have an important implication concerning the practical implementation of such a methodology due to the nature of how the hemolysis solution varies across operating conditions. As shown here, if shear stress is varied but exposure time is fixed, we obtain a unique value of b. But, an infinite number of combinations of C and a defined along a line in (C, a, b) parameter space (e.g., the line of intersection shown in Fig. 4b) may be used to match experimental hemolysis measurements. Similarly, if exposure time is varied and shear stress is fixed, we obtain a unique value of a, but an infinite number of combinations of C and b may be used to match experiments (e.g., see Fig. 4c). Thus, at least for planar Couette flow, to obtain a unique set of power law coefficients for a specific device using a particular species of animal blood, we must vary both shear stress and exposure time.

Using this approach, we determine device- and species-specific power law coefficients for planar Couette flow using bovine blood as follows. We first calculate the IH_{outlet} response field from analytical solutions of the Eulerian power law model at three conditions that span a range of shear stress and exposure time values ($\sigma = 50\,\text{Pa}$, $t_{\text{exp}} = 1.2\,\text{s}$;

$\sigma = 150\,\text{Pa}, t_{\text{exp}} = 0.25\,\text{s}$; $\sigma = 250\,\text{Pa}, t_{\text{exp}} = 0.05\,\text{s}$). For each condition, we extract an isosurface of IH_{outlet} that corresponds to the experimental value calculated from the empirical correlation of Ding et al. (2015) for bovine blood at the same shear stress and exposure time. We then search for common points of intersection among all three isosurfaces that correspond to unique values of C, a, and b that yield hemolysis solutions that match the experiments at all three conditions. In practice, we found that this is most easily accomplished by performing a Boolean intersection of two of the isosurfaces and repeating this for each of the three combinatorial pairs available among the three isosurfaces. This yields a set of three lines of intersection (one for each combinatorial pair of the three isosurfaces) that are easily interrogated for any common points of intersection.

As shown in Fig. 5a, for any two conditions the experimental isosurfaces intersect to form a curve—or line of intersection—in (C, a, b) parameter space along which an infinite number of combinations of C, a, and b are defined

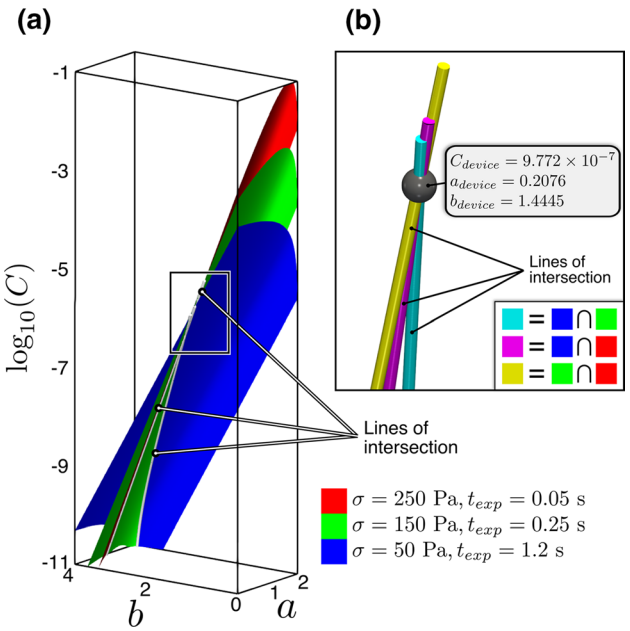

Fig. 5 Device- and species-specific hemolysis power law coefficients for planar Couette flow. **a** Isosurfaces of IH_{outlet} in (C, a, b) parameter space extracted from analytical solutions of the Eulerian power law model that correspond to values from the experimental correlation of Ding et al. (2015) for IH_{sp} in a Couette-type shearing device at three conditions using bovine blood. The intersection of each isosurface with the others was calculated and is illustrated here as lines of intersection. **b** Enlarged view of the inset shown in panel a depicting the lines of intersection between the three isosurfaces, with the lines color-coded by the two isosurfaces that form the intersection (e.g., the cyan line of intersection is formed by the intersection of the blue and green isosurfaces in **a**). As illustrated, the three lines of intersection themselves intersect at a common point in (C, a, b) parameter space that corresponds to the location of the device- and species-specific power law coefficients, denoted as $(C, a, b)_{\text{device}}$

that yield hemolysis solutions that match the experimental value at both conditions. Boolean intersection of the three available combinatorial pairs of isosurfaces yields a set of three lines of intersection. As illustrated in Fig. 5b, the three lines of intersection themselves intersect at a single common point that defines the location in (C, a, b) parameter space where Eulerian power law model solutions match values calculated from the experimental correlation of Ding et al. (2015) at all three conditions—i.e., the device-specific power law coefficients for this particular species of animal blood, denoted $(C, a, b)_{\text{device}}$. In this manner, the device-specific power law coefficients are determined to be: $C_{\text{device}} = 9.772 \times 10^{-7}$, $a_{\text{device}} = 0.2076$, and $b_{\text{device}} = 1.4445$, which are identical to the empirical coefficients of Ding et al. (2015) for bovine blood. This confirms that, at least for planar Couette flow, this approach may be used to determine device- and species-specific hemolysis power law coefficients. Note, however, that it requires the analysis of multiple operating conditions that span a range of shear stress and exposure time values to determine a single unique set of device-specific coefficients, which has several practical implications that are addressed in the following sections.

4.2 Analytical: circular Poiseuille flow

We next apply the foregoing approach to circular Poiseuille flow, a case with non-uniform shear conditions where a global empirical power law is more difficult to define due to the lack of a single characteristic value of shear stress with a corresponding exposure time.

4.2.1 Analytical solution

Assuming steady-state, axisymmetric fully developed flow with no-slip conditions at the boundaries, the classical Poiseuille solution for the velocity distribution in a tube of circular cross section is:

$$u_x(r) = -\frac{R^2}{4\mu}\frac{\mathrm{d}p}{\mathrm{d}x}\left(1 - \frac{r^2}{R^2}\right) \tag{16}$$

where $u_x(r)$ is the axial velocity as a function of the radial coordinate r, R is the radius of the tube, and $\mathrm{d}p/\mathrm{d}x$ is the applied pressure gradient along the tube. For convenience, Eq. 16 can also be written in terms of the average cross-sectional velocity, defined as

$$U_{\text{avg}} = \frac{1}{\pi R^2}\int_0^{2\pi}\int_0^{R} u_x(r)\, r\, dr\, d\theta = -\frac{R^2}{8\mu}\frac{\mathrm{d}p}{\mathrm{d}x} \tag{17}$$

which yields

$$u_x(r) = 2U_{\text{avg}}\left(1 - \frac{r^2}{R^2}\right). \tag{18}$$

This parabolic velocity profile yields a linear viscous scalar stress, calculated from Eqs. 6–8 as:

$$\sigma = \left|\frac{r}{2}\frac{\mathrm{d}p}{\mathrm{d}x}\right| = \left|\frac{4\mu U_{\mathrm{avg}} r}{R^2}\right|. \tag{19}$$

Given the velocity and stress distributions in the tube and assuming an inlet plasma free hemoglobin fraction of zero ($H(x=0,r)=0$), the analytical solution of the Eulerian power law model (Eq. 5) is:

$$\begin{aligned} H(x,r) &= C\,\sigma^b\left(\frac{x}{u_x(r)}\right)^a \\ &= C\left|\frac{4\mu U_{\mathrm{avg}} r}{R^2}\right|^b\left(\frac{x}{2U_{\mathrm{avg}}\left(1-\frac{r^2}{R^2}\right)}\right)^a \end{aligned} \tag{20}$$

where x is the distance from the inlet in the axial direction (see Fig. 3b). Finally, the index of hemolysis at the tube outlet, IH_{outlet}, is calculated as the integrated flux of $H(x, r)$ at the outlet, located at $x = L$, normalized by the integrated outlet flow rate (Eq. 11), yielding a closed-form analytical solution

$$\begin{aligned} IH_{\mathrm{outlet}} &= \frac{\int_{\mathrm{outlet}} (H\,\mathbf{u})\cdot \mathrm{d}\mathbf{A}}{\int_{\mathrm{outlet}} \mathbf{u}\cdot \mathrm{d}\mathbf{A}} \\ &= 2C\left(\frac{L}{2U_{\mathrm{avg}}}\right)^a\left(\frac{4\mu U_{\mathrm{avg}}}{R}\right)^b \\ &\quad \left.\frac{\Gamma(2-a)\Gamma\left(1+\frac{b}{2}\right)}{\Gamma\left(3-a+\frac{b}{2}\right)}\right|_{b>-2\,\wedge\, a<2} \end{aligned} \tag{21}$$

that is confined to a restricted domain in (C, a, b) parameter space with $b > -2$ and $a < 2$. Here, $\Gamma(z)$ is the Euler gamma function, $C, a, b, L, R, \mu, U_{\mathrm{avg}} \in \mathbb{R}$, and $L, R, \mu, U_{\mathrm{avg}} > 0$.

4.2.2 Behavior of hemolysis solution

Given the analytical expression in Eq. 21, we can map the hemolysis response field from the Eulerian power law model in (C, a, b) parameter space. To compare with experiments, here we leverage the hemolysis data of Kameneva et al. (2004) acquired using a recirculating suspension of bovine red blood cells flowing through a small capillary tube with a radius of 0.5 mm and a length of 70 mm. Because the experiments of Kameneva et al. (2004) are multi-pass, we convert the reported values of plasma free hemoglobin concentration to values of *MIH* using Eq. 10 (see "Appendix 2" for details).

As described in Sect. 3.3, to directly compare the Eulerian power law model results with experimental values of *MIH*, we scale IH_{outlet} by 10^6. In this way, we calculate analytical solutions of *MIH* for steady, axisymmetric fully developed laminar flow in a capillary tube of the same dimensions and with flow at the same average wall shear conditions ($\overline{\sigma}_{\mathrm{wall}}$ of 200, 300, and 400 Pa) as reported by Kameneva et al. (2004). At each operating condition, we use the analytical solution of Eq. 21 to map *MIH* as a function of C, a, and b. As before, we then extract the value of *MIH* that matches the experimental *MIH* value of Kameneva et al. (2004) at the same conditions. Importantly, at each condition, we also consider the uncertainty in the experimental hemolysis measurements by extracting the *MIH* values associated with the reported standard deviation in the measured mean value.

Considering the behavior of the hemolysis solution at a single condition, the variation in the *MIH* response field for circular Poiseuille flow is similar to the variation in IH_{outlet} observed for planar Couette flow. As shown in Fig. 6a, *MIH* varies smoothly from a value approaching zero as C and b approach zero, to extremely large, non-physical values at the opposite corner of the (C, a, b) parameter space domain. As discussed in Sect. 3.3, *MIH* cannot physically exceed a value of 10^6. As observed from Fig. 6a, however, the present form of the Eulerian power law model yields highly non-physical solutions ($MIH \gg 10^6$) for large values of C and b.

Similar to planar Couette flow, at a single operating condition the extracted values of *MIH* that match the mean experimental hemolysis data form a continuous isosurface that sweeps through the (C, a, b) parameter space (Fig. 6a). Here, however, we also account for the uncertainty in the hemolysis measurements by extracting isosurfaces of *MIH* that correspond to the reported standard deviation in the experiments ($MIH = 28.84 \pm SD$ in Fig. 6a). The two bounding $\pm SD$ isosurfaces sweep a small volume in (C, a, b) parameter space wherein the Eulerian power law model results fall within the uncertainty bounds of the experimental data. That is, any combination of C, a, and b within this small volume may be used in the Eulerian power law model to yield hemolysis results that match the experimental data to within the uncertainty of the measurements.

To characterize how the hemolysis solution varies over multiple conditions, we extract isosurfaces of *MIH* that correspond to the mean experimental measurements of Kameneva et al. (2004) at three operating conditions ($\overline{\sigma}_{\mathrm{wall}}$ of 200, 300, and 400 Pa). As shown in Fig. 6b, c, Boolean intersection of the three available combinatorial pairs of isosurfaces yields a set of three lines of intersection. Unlike the foregoing Couette flow case, however, the three lines of intersection themselves do not intersect at a single common point, indicating that there is not a single unique set of power law coefficients for this case that may be used to

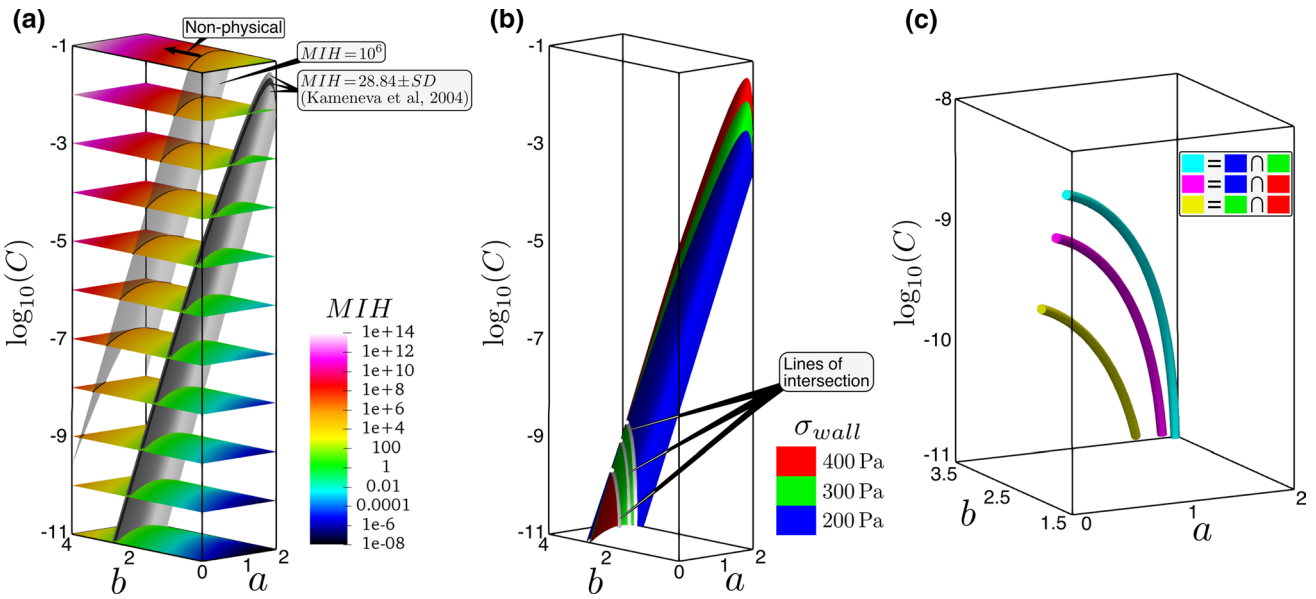

Fig. 6 Device- and species-specific hemolysis power law coefficients for circular Poiseuille flow. **a** Map of the modified index of hemolysis, *MIH*, in (*C*, *a*, *b*) parameter space for a single operating condition ($\sigma_{\text{wall}} = 400\,\text{Pa}$). An isosurface of $MIH = 10^6$ is shown as the delineation between physical ($MIH \leq 10^6$) and non-physical ($MIH > 10^6$) hemolysis solutions. Isosurfaces of $MIH = 28.84 \pm SD$ are also shown, which correspond to the experimental hemolysis measurements of Kameneva et al. (2004) in a small capillary tube with $\overline{\sigma}_{\text{wall}} = 400\,\text{Pa}$ using a suspension of bovine red blood cells. The dark gray isosurface corresponds to the measured mean value, and the light gray isosurfaces correspond to the mean value plus and minus one standard deviation (*SD*). **b** Isosurfaces of *MIH* that correspond to the mean experimental measurements of Kameneva et al. (2004) at three operating conditions ($\overline{\sigma}_{\text{wall}}$ of 200, 300, and 400 Pa). The intersection of each of the isosurfaces was calculated and is illustrated here as lines of intersection. **c** Enlarged view of the lines of intersection depicted in **b**, with the lines color-coded by the two isosurfaces that form the intersection (e.g., the magenta line of intersection is formed by the intersection of the blue and red isosurfaces in **b**). As illustrated, the three lines of intersection themselves do not intersect at a common point in (*C*, *a*, *b*) parameter space (see the main text for details and the implications)

predict hemolysis levels that match the *mean* hemolysis data of Kameneva et al. (2004) at all three conditions.

4.2.3 Generalized approach for determining device-specific coefficients

The lack of a single unique set of device-specific coefficients for fully developed flow in the capillary tube is likely due to the limited range of shear stress and exposure time values across the three operating conditions. In the foregoing Couette flow case, we observed that both shear stress and exposure time must span a relatively wide range of values in order for the extracted experimental isosurfaces to shift appreciably enough such that they intersect at a common point. To obtain a single unique set of device-specific coefficients for planar Couette flow, the shear stress was varied by a factor of 5 ($\sigma = 50 - 250\,\text{Pa}$) and exposure time was varied by a factor of 24 ($t_{\text{exp}} = 0.05 - 1.2\,\text{s}$). This range of values corresponds to the approximate range of shear stress and exposure time in the experiments of Ding et al. (2015), which was made possible by using two Couette-type shearing devices (one for low shear and one for high shear conditions) and by independently controlling the rotational speed of the rotor and the flow rate through each device. In this way, a wide range of flow conditions was achieved, ranging from low shear with a short exposure time (using a slow rotational speed and a high flow rate) to high shear with a long exposure time (using a fast rotational speed and a low flow rate). In contrast, because the capillary tube length is fixed in the present case and only the flow rate changes between conditions, the shear stress and exposure time cannot be independently controlled, thereby limiting the range of values that are obtainable—here, both the wall shear stress and the average exposure time vary by only a factor of 2 ($\sigma_{\text{wall}} = 200 - 400\,\text{Pa}$ and average $t_{\text{exp}} = 0.0088 - 0.0176\,\text{s}$). As a result, the extracted *MIH* isosurfaces in Fig. 6b do not shift appreciably enough across conditions such that they all intersect at a common point in (*C*, *a*, *b*) parameter space.

How, then, can we determine an appropriate set of device-specific coefficients for the capillary tube? Given the uncertainty in the experimental measurements, it turns out that it is not critical that the extracted mean *MIH* isosurfaces do not intersect at a common point to give a single, unique set of device-specific coefficients. In fact, there is a range of coefficients that may be used in the Eulerian power law model to match experiments at all conditions to within the uncertainty of the measurements. This range of coefficients is defined by a small envelope in (*C*, *a*, *b*) parameter

space that encompasses hemolysis values that fall within the uncertainty bounds of the experimental data, identified here by the isosurfaces corresponding to the measured mean *MIH* plus and minus one SD at each condition (see Fig. 6a). We note that all three lines of intersection shown in Fig. 6b, c are contained within this envelope and that the magenta line, formed by the intersection of the 200 Pa and 400 Pa isosurfaces (blue and red isosurfaces in Fig. 6b, respectively), passes through approximately the center of the envelope. Accordingly, to quantify a set of appropriate device-specific coefficients we can fit a parametric curve to the 200–400 Pa line of intersection. This is the approach that we use to calculate device- and species-specific coefficients for the capillary tube in Sect. 4.3, where we eliminate the primary limitation of the present analysis—the assumption of fully developed flow—and use CFD and Kriging surrogate modeling in lieu of analytical solutions to map the hemolysis response field.

4.3 Numerical: device-specific coefficients for developing flow in a small capillary tube

In general, exact analytical solutions of flow and hemolysis in a real medical device do not exist, thus requiring an alternative approach to map the hemolysis response field in (C, a, b) parameter space. Here we use CFD-based Kriging surrogate modeling. Analytical solutions have, nonetheless, proved to be valuable in elucidating the nature of the Eulerian power law model solution and for establishing a methodology for determining device-specific coefficients. Importantly, in Sects. 4.1 and 4.2 we showed that there is not a unique global optimum in the hemolysis response field at a single condition for both planar Couette flow and circular Poiseuille flow. Accordingly, standard optimization techniques cannot be utilized to obtain device-specific power law coefficients by minimizing an objective function at a single operating condition (e.g., see Algorithm 2 and related discussion). Thus, here we use Kriging interpolation to construct a globally accurate surrogate model of the hemolysis field in (C, a, b) parameter space from CFD data obtained from simulations performed using the previously verified hemolysis solver developed in OpenFOAM (Sect. 3.4). The globally accurate surrogate model is then explored and, as before, device-specific values of C, a, and b are identified by extracting isosurfaces of *MIH* that correspond to experimental hemolysis measurements at the same conditions. In "Appendix 3," we present the results of a verification study performed to assess the accuracy of our CFD-based Kriging surrogate modeling framework by comparing with analytical solutions for circular Poiseuille flow. Here, we apply our verified Kriging surrogate modeling approach to predict the device- and species-specific coefficients for developing laminar flow in the capillary tube of Kameneva et al. (2004).

The primary limitation of the forgoing analytical analysis for circular Poiseuille flow in Sect. 4.2 is our assumption of fully developed flow in the capillary tube. In reality, the flow is not fully developed along the entire length of the tube in the experiments of Kameneva et al. (2004). The fully developed flow assumption was invoked to obtain an analytical solution that was used to map the continuous hemolysis response field in (C, a, b) parameter space to: (i) understand the nature of the solution and to develop a generalized approach for predicting device-specific power law coefficients (Sect. 4.2) and (ii) to verify our CFD-based Kriging surrogate modeling framework (see "Appendix 3"). However, at the conditions of the experiments the flow is not entirely fully developed, particularly at the higher flow rate conditions. According to White (2011), the accepted correlation for the entrance length for laminar flow in a tube is $L_e/d \approx 0.06\,Re_D$. In the experiments of Kameneva et al. (2004), at the lower flow rate condition with $\overline{\sigma}_{\text{wall}} = 200\,\text{Pa}$ the reported Reynolds number, Re_D, is 550. Thus, the entrance length is estimated to be 33 mm. Given that the capillary tube length is 70 mm, 47% of the upstream length contains developing flow. At the highest flow rate condition with $\overline{\sigma}_{\text{wall}} = 400\,\text{Pa}$, the reported Re_D is 1000 and the entrance length is calculated to be 60 mm. Thus, approximately 86% of the upstream length contains developing flow and only 14% of the length near the capillary tube outlet contains fully developed flow.

To determine the device-specific coefficients requires consideration of the developing flow and hemolysis in the entry region of the tube, a case for which an analytical solution does not exist, thus requiring the use of our CFD-based Kriging surrogate modeling framework. To obtain developing flow conditions that replicate the experiments of Kameneva et al. (2004), we constructed a CFD model of the capillary tube that includes the large inlet contraction that was placed upstream of the tube in the experimental flow loop (see "Appendix 4"). We also included a short (1 cm) straight inlet tube upstream of the contraction and applied fully developed flow conditions at the upstream inlet with a pressure drop equal to that measured in the experiments (see "Appendix 2"). Steady-state axisymmetric CFD simulations were then performed to replicate the developing flow conditions present in the capillary tube at each operating condition ($\overline{\sigma}_{\text{wall}}$ of 200, 300, and 400 Pa). To ensure the accuracy of the CFD simulations, we also performed a mesh refinement study, the results of which are presented in "Appendix 4".

Given the computed steady-state flow solution at each condition, we use our verified CFD-based Kriging surrogate modeling framework to predict the device-specific power law coefficients for the developing laminar flow of a suspension of bovine red blood cells through the capillary tube. Qualitatively, we observe that the behavior of the hemolysis solution at a single operating condition (Fig. 7a) is similar

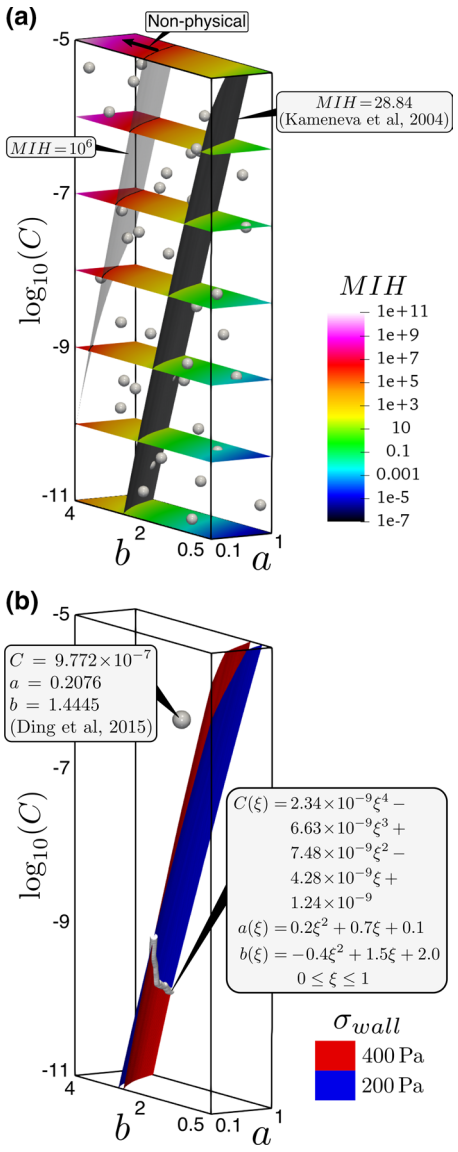

Fig. 7 Device- and species-specific hemolysis power law coefficients for developing laminar flow of a suspension of bovine red blood cells through a small capillary tube calculated using CFD-based Kriging surrogate modeling. **a** Map of the modified index of hemolysis, *MIH*, in (C, a, b) parameter space for a single operating condition ($\overline{\sigma}_{\text{wall}} = 400$ Pa). The 40 CFD sample points used to construct the surrogate model are shown. An isosurface of $MIH = 28.84$ is also shown, which corresponds to the mean experimental data of Kameneva et al. (2004) from hemolysis measurements in a small capillary tube with $\overline{\sigma}_{\text{wall}} = 400$ Pa using a suspension of bovine red blood cells. The isosurface of $MIH = 10^6$ illustrates the delineation between physical ($MIH \leq 10^6$) and non-physical ($MIH > 10^6$) hemolysis solutions. **b** Line of intersection obtained by performing a Boolean intersection of the isosurfaces of *MIH* extracted from the computed hemolysis response field corresponding to the mean experimental measurements of Kameneva et al. (2004) at two operating conditions ($\overline{\sigma}_{\text{wall}}$ of 200 and 400 Pa). A parametric curve fit of the 200–400 Pa line of intersection yields: $C(\xi) = 2.34 \times 10^{-9}\xi^4 - 6.63 \times 10^{-9}\xi^3 + 7.48 \times 10^{-9}\xi^2 - 4.28 \times 10^{-9}\xi + 1.24 \times 10^{-9}$, $a(\xi) = 0.2\xi^2 + 0.7\xi + 0.1$, and $b(\xi) = -0.4\xi^2 + 1.5\xi + 2.0$, where ξ is the parametric variable defined as $0 \leq \xi \leq 1$. For comparison, the location of the power law coefficients of Ding et al. (2015) obtained from measurements in a Couette-type shearing device using bovine blood is also shown

to that observed for both planar Couette flow and circular Poiseuille flow, which includes the presence of highly non-physical solutions at large values of C and b. To calculate device-specific coefficients, we computed surrogate model predictions at all three conditions ($\overline{\sigma}_{\text{wall}}$ of 200, 300, and 400 Pa). We then extracted isosurfaces corresponding to the hemolysis measurements of Kameneva et al. (2004) at each condition, performed a Boolean intersection of each of the isosurfaces, and calculated the lines of intersection that are used to determine the device-specific coefficients (see Sect. 4.2). This yields the 200–400 Pa line of intersection shown in Fig. 7b. To quantify a set of appropriate device-specific coefficients, we fit a parametric curve to the 200–400 Pa line of intersection, yielding

$$\begin{aligned} C(\xi) &= 2.34 \times 10^{-9}\xi^4 - 6.63 \times 10^{-9}\xi^3 \\ &\quad + 7.48 \times 10^{-9}\xi^2 - 4.28 \times 10^{-9}\xi + 1.24 \times 10^{-9}, \\ a(\xi) &= 0.2\xi^2 + 0.7\xi + 0.1, \\ b(\xi) &= -0.4\xi^2 + 1.5\xi + 2.0 \end{aligned} \tag{22}$$

where ξ is the parametric variable defined as $0 \leq \xi \leq 1$. As shown in Sect. 4.2 for circular Poiseuille flow, the 200–400 Pa line of intersection passes through approximately the center of the small envelope in (C, a, b) parameter space that encompasses hemolysis values corresponding to the uncertainty bounds of the experimental data at all three conditions ($\overline{\sigma}_{\text{wall}}$ of 200, 300, and 400 Pa). Thus, this parametric curve defines a set of device-specific hemolysis power law coefficients for the developing laminar flow of a suspension of bovine red blood cells through a small capillary tube that yields hemolysis predictions that match the measurements of Kameneva et al. (2004) to within the reported uncertainty in the experiments.

Comparing the device-specific coefficients defined along this parametric curve with the power law coefficients of Ding et al. (2015) from measurements in a Couette-type shearing device using bovine blood, there is a large difference—particularly in the values of the C and b coefficients. This large difference is dramatically illustrated in Fig. 7b, where we also plot the location of the power law coefficients of Ding et al. (2015) in (C, a, b) parameter space. As shown, the range of the a coefficient ($0.1 \leq a \leq 1$) encompasses the value of 0.2076 from Ding et al. (2015); however, the range of both the C and b coefficients do not encompass the Ding et al. (2015) values. From the parametric equation (Eq. 22), the coefficient b, which has a range of $2.0 \leq b \leq 3.1$, is comparatively larger than the value of 1.4445 from Ding et al. (2015). More significantly, however, the C coefficient, which has a range of $1.5 \times 10^{-10} \leq C \leq 1.24 \times 10^{-9}$, is between about 800 and 6500 times less than the C coefficient of Ding et al. (2015). Since both experiments use bovine red blood cells, these differences are not due to species differences in

RBC fragility. Rather, the differences are more likely due to device-specific differences in the flow conditions—in particular, the uniform versus non-uniform shear conditions present in Couette versus developing pipe flow, respectively.

Such large differences in the power law coefficients raises the important practical question of how inaccurate the Eulerian power law model solution would be if we were to use the coefficients of Ding et al. (2015) to predict hemolysis in the capillary tube of Kameneva et al. (2004). From the *MIH* map for developing pipe flow with $\overline{\sigma}_{\text{wall}} = 400$ Pa (Fig. 7a), we extract the *MIH* value in (C, a, b) parameter space corresponding to the Ding et al. (2015) coefficients for bovine blood. This yields an *MIH* value of 609, compared with $MIH = 29 \pm 9$ from the hemolysis experiments of Kameneva et al. (2004) (see "Appendix 2"). That is, using the Ding et al. (2015) power law coefficients, developed from uniform shear experiments, in the Eulerian power law model to compute hemolysis for developing laminar flow in the capillary tube of Kameneva et al. (2004), we obtain a prediction of *MIH* that is in error by more than 2000% compared to the experimental measurements. This highlights the inadequacy of the traditional approach of using idealized coefficients obtained from simplified experiments under uniform shear conditions to predict hemolysis even for the relatively simple non-uniform shear flow present in a capillary tube.

5 Discussion

In this study, we develop a novel approach for determining device- and species-specific hemolysis power law coefficients. We choose to use a form of the Eulerian power law model that permits the derivation of analytical solutions for simplified cases (planar Couette flow and circular Poiseuille flow), allowing us to develop and verify our generalized methodology using analytical methods. We then extend our generalized approach to more practical cases relevant to blood-contacting medical devices wherein analytical solutions are unavailable. Here, we replace the requirement for an analytical solution in our generalized approach with CFD-based Kriging surrogate modeling, which we also verify by comparing with the results obtained using exact analytical solutions. Finally, we apply our verified CFD-based Kriging surrogate modeling approach to predict the device- and species-specific hemolysis power law coefficients for developing laminar flow in the small capillary tube of Kameneva et al. (2004). We strategically choose this case because it contains appreciable non-uniform stress due to laminar flow in a relatively simple geometry, allowing us to have a high degree of confidence in our CFD simulations and to avoid the complications of turbulence modeling and the uncertainties associated with the influence of turbulence on hemolysis. We find that the device- and species-specific hemolysis power law coefficients for the capillary tube are much different than traditional empirical coefficients obtained from Couette-type device with uniform shear flow, and that using such idealized traditional coefficients yields a highly inaccurate prediction of hemolysis that is in error by more than 2000% compared to experimental measurements.

The CFD-based Kriging surrogate modeling approach that we present here is a powerful practical tool for determining device- and species-specific hemolysis power law coefficients in blood-contacting medical devices. It may be readily used to determine empirical power law coefficients in complex devices (e.g., blood pumps, heart valves) for any species of animal blood. To date, determining such coefficients in devices with complex flow fields and highly non-uniform flow-induced stress has been challenging due to the ambiguity of defining a characteristic stress and exposure time (see Sect. 1 for related discussion). We envision that our approach may be leveraged in two ways:

1. In the near term, our approach may be used to assemble a database of device- and species-specific empirical coefficients for the power law model for a range of devices and species of animal blood. This database of coefficients may then be used as a resources by others, who can select the most appropriate set of empirical coefficients to characterize the hemolytic potential of their device using the power law model. This is the approach that we propose in Fig. 1b. While the applicability of our proposed approach of applying device-specific coefficients from one device to predict the hemolytic potential of a second, similar device needs to be assessed in future work, we believe that it represents an advance over the traditional approach of using idealized global empirical coefficients derived from simplified uniform shear experiments in complex medical devices (Fig. 1a). Indeed, as we demonstrate in Sect. 4.3, this traditional approach yields extremely poor predictions of hemolysis even in a relatively simple capillary tube. We believe that, in the near term, our proposed approach may be used in lieu of the traditional approach to improve the predictive accuracy of the hemolysis power law model until more advanced physics-based models are developed.
2. In the intermediate and long term, our CFD-based Kriging surrogate modeling framework may be used to determine empirical coefficients in more advanced hemolysis models. As demonstrated here and noted by others, the standard power law model has a number of deficiencies that include the possibility of highly non-physical solutions, a lack of universal empirical coefficients that may be used to accurately predict hemolysis in different devices, the inability to account for accumulated damage to RBCs (Grigioni et al. 2004), and use of a scalar stress

that is unable to account for differences in hemolysis due to shear versus extensional stress (Faghih and Sharp 2018). In the future, more advanced physics-based models should be developed that address each of these limitations to enable more accurate prediction of absolute hemolysis levels in blood-contacting medical devices. Importantly, our CFD-based Kriging surrogate modeling framework is not restricted to the power law model. It may be used to determine empirical coefficients that will undoubtedly exist in new and improved continuum-scale hemolysis models. More generally, we note that our approach may also be used to determine coefficients used in models of other forms of flow-induced blood damage—e.g., platelet activation (Alemu and Bluestein 2007; Bodnár 2014) and thrombosis (Taylor et al. 2016). Depending on the form of the blood damage model and the behavior of the solution, a unique global optimum may exist in the response field for a single operating condition. In this case, the optimization option present in our Kriging surrogate modeling framework (Algorithm 2) may be used to minimize an objective function to automatically find the location of the global optimum, thereby obviating the need to extract isosurfaces of the response field across multiple conditions and search for common points of intersection.

To our knowledge, this study represents the first rigorous description of an approach to quantify device-specific empirical coefficients for a hemolysis model in a device with non-uniform shear flow. A previous study by Fraser et al. (2012) used CFD and the same Eulerian power law model presented here to predict hemolysis in five ventricular assist devices (VADs). Using idealized global empirical coefficients from the literature, they note that in previous work their CFD hemolysis predictions considerably overpredicted experimental measurements. Because of this, they instead used a "gradient descent algorithm" to fit CFD predictions to experimental data from two of the VADs to develop an improved set of power law coefficients that were used in subsequent simulations. This is similar in spirit to the approach presented here. However, Fraser et al. (2012) provide no details regarding their approach. Thus, it is unclear how they determined coefficients that yield hemolysis predictions that best match experimental data. Further, the nature of the hemolysis response field in (C, a, b) parameter space is not presented or discussed, and so it is unclear whether a unique global optimum exists for their VADs that yields a single, unique set of power law coefficients or whether their gradient descent approach located a local optimum. Here, we propose a comprehensive approach for determining device- and species-specific hemolysis power law coefficients that may be readily applied to VADs.

The analytical hemolysis solutions derived in this study also represent a new theoretical contribution. Previous work by Hariharan et al. (2015) derived closed-form analytical Eulerian power law model solutions for profiles of the plasma free hemoglobin fraction for two of the same benchmark cases presented here (planar Couette flow and circular Poiseuille flow). However, they stop short of deriving a closed-form analytical solution for the integrated index of hemolysis at the outlet of the device, IH_{outlet}, and mapping the hemolysis response field in (C, a, b) parameter space, as we do here.

Lastly, we note a couple limitations of the present study. For the reasons described in Sect. 2, we demonstrate our CFD-based Kriging surrogate modeling approach in a relatively simple capillary tube geometry. Future work should apply our approach in more complex blood-contacting medical devices (e.g., Malinauskas et al. 2017; Hariharan et al. 2018). However, as other researchers have pointed out (Yu et al. 2017; Malinauskas et al. 2017), credible hemolysis data from well-controlled experimental studies of different flow models and devices are lacking. More credible data are needed to develop device-specific hemolysis power law coefficients in complex medical devices and to assess our proposed approach of applying device-specific coefficients from one device to predict the hemolytic potential of a second, similar device (Fig. 1b).

Finally, we note that our approach is somewhat computationally expensive, as we found that it requires 40 CFD simulations per operating condition to accurately map the hemolysis response field in (C, a, b) parameter space. The Kriging prediction steps of the analysis (steps 5 and 6 in Algorithm 2) are relatively inexpensive, requiring only about 2–3 h to complete in the present study. The remaining wall clock time (i.e., elapsed physical time) is spent in performing the requisite CFD simulations. However, because our framework is developed to run in a parallel computing environment, individual calculations in each batch of CFD simulations can be run concurrently. Given adequate computational resources, this significantly reduces the total wall clock time required to obtain a surrogate model prediction. In this study, our CFD-based Kriging surrogate modeling framework required approximately 7–8 h of wall clock time on a high-performance computing (HPC) system at the US Food and Drug Administration to compute the hemolysis response field for each operating condition for the capillary tube geometry (Sect. 4.3). While it will require more computational resources and potentially longer wall clock times, performing CFD-based Kriging surrogate modeling for complex devices is certainly feasible on modern HPC systems.

6 Summary and conclusions

Most stress-based power law models used in CFD leverage the global empirical correlation first proposed by Giersiepen et al. (1990) that relates hemolysis generation and the flow-induced stress and exposure time. Both Lagrangian and Eulerian forms of the power law model are derived by recasting the global correlation to a local formulation that still requires empirical coefficients (C, a, and b). In the absence of more appropriate values, investigators typically utilize coefficients obtained by fitting the global correlation of Giersiepen et al. (1990) using hemolysis data acquired in simplified Couette-type shearing devices under uniform shear conditions and with well-defined exposure times. CFD simulations that use these idealized global empirical coefficients are then performed to predict the hemolytic potential of a medical device with a complex hemodynamic flow field that includes highly non-uniform stress and where there is not a well-defined exposure time.

The applicability of this traditional approach of using idealized empirical coefficients to predict hemolysis in complicated blood-contacting medical devices (Fig. 1a) is currently unknown. The wide range of power law coefficients reported in the literature seems to indicate that coefficients are device-specific and dependent on the species of animal blood. This may partially explain why it is so challenging to accurately predict absolute hemolysis levels using coefficients from simplified experiments. In application, however, if power law coefficients are device- and species-specific, it is currently unclear how to best determine reliable coefficients—particularly for complicated devices with highly non-uniform flow-induced stress and where there is not a well-defined exposure time.

In this study, we propose a new approach for determining device- and species-specific hemolysis power law coefficients (Fig. 1b). Given detailed quantification of the flow field in a device, multiple power law model solutions are calculated using different sets of coefficients to map the hemolysis response field in three-dimensional (C, a, b) parameter space. We then compare the hemolysis response field predictions with available experimental data in the same device to determine the power law coefficients that, when incorporated into the locally defined power law model, yield correct global hemolysis predictions for a particular device and with a particular species of animal blood (i.e., device- and species-specific coefficients). We first develop this approach by deriving analytical solutions for simple uniform and non-uniform shear flows (planar Couette flow and circular Poiseuille flow, respectively) that allow us to continuously map the hemolysis solution in (C, a, b) parameter space for each case. Given the unavailability of analytical solutions for flow and hemolysis in real devices, we next develop and verify a practical approach to map the hemolysis response field using CFD and Kriging surrogate modeling. To demonstrate the utility of the approach, we replicate the flow conditions present in the hemolysis experiments of Kameneva et al. (2004) and use our CFD-based Kriging surrogate modeling framework to determine device- and species-specific power law coefficients for the laminar flow of a recirculating suspension of bovine red blood cells through a small capillary tube. The resultant coefficients are compared with traditional coefficients derived from Couette-type devices under uniform shear conditions. Finally, the accuracy of the traditional approach of using the Eulerian power law model with idealized global empirical coefficients to predict hemolysis in the capillary tube is examined.

Our analytical analyses reveal that there is not a single, unique set of device-specific coefficients that yields a hemolysis solution that matches experiments at a single operating condition. For both uniform and non-uniform shear cases (planar Couette flow and circular Poiseuille flow, respectively), the extracted hemolysis response field solutions that match experimental data form a continuous isosurface that sweeps through the (C, a, b) parameter space. This is significant for two reasons: (i) at a single operating condition, an infinite number of combinations of power law coefficients defined along a common isosurface may be used to match experimental data and (ii) because a unique global optimum does not exist, standard optimization techniques cannot be utilized to obtain device-specific power law coefficients by minimizing an objective function at a single operating condition. This informed our approach for determining device-specific coefficients.

Using analytical solutions for planar Couette flow and circular Poiseuille flow, we developed a generalized methodology for determining device- and species-specific hemolysis power law coefficients. We first calculate the hemolysis response field at multiple operating conditions that span a range of shear stress and exposure time values. For each condition, we extract an isosurface of the hemolysis field prediction (IH_{outlet}) that matches experimental hemolysis measurements of IH_{sp} or MIH from single-pass or multi-pass experiments, respectively. We then perform a Boolean intersection of each of the isosurfaces and search for common points of intersection that correspond to unique values of C, a, and b that yield hemolysis solutions that match the experiments at all conditions (i.e., the device- and species-specific coefficients).

Employing this approach, we determined the device-specific hemolysis power law coefficients for the developing laminar flow of a suspension of bovine red blood cells in the small capillary tube of Kameneva et al. (2004)—a case for which an analytical solution does not exist, requiring the use of our CFD-based Kriging surrogate modeling framework.

Unlike the foregoing Couette flow case, we found that there is not a single, unique set of device-specific power law coefficients for the capillary tube that may be used to predict hemolysis levels that match *mean* experimental measurements at all conditions. We found that this is likely due to the limited range of shear stress and exposure time values across the operating conditions considered by Kameneva et al. (2004). Though seemingly disconcerting, this has important practical implications, as it is also likely to be the case in other medical devices in which flow-induced stress and exposure time do not vary appreciably across conditions. Furthermore, it is unavoidable if we also consider the uncertainty in the experimental measurements. To overcome this difficulty and to demonstrate a practical approach, we calculated a set of device- and species-specific coefficients by fitting the parametric curve formed by the intersection of the two isosurfaces corresponding to the extreme conditions: low shear/long exposure time and high shear/short exposure time. We show that this parametric curve defines a set of power law coefficients that yield hemolysis predictions that match the experimental data of Kameneva et al. (2004) to within the reported uncertainty of the measurements at all three conditions that we considered.

Compared with traditional coefficients, the device-specific coefficients that we determined for the capillary tube of Kameneva et al. (2004) are much different than the idealized global empirical coefficients reported by Ding et al. (2015) from experiments in Couette-type shearing devices under uniform shear conditions. In particular, the range of the device-specific b coefficient is comparatively larger than the Ding et al. (2015) coefficient for bovine blood. More significantly, however, the range of the C coefficient is between about 800 and 6500 times less than the C coefficient of Ding et al. (2015). Because both Ding et al. (2015) and Kameneva et al. (2004) used bovine red blood cells, these differences are not due to species differences in RBC fragility. It is difficult to precisely compare the Ding et al. (2015) and Kameneva et al. (2004) data due to differences in the experiments (single-pass vs. multi-pass, short- vs. long-time duration, 30% vs. 24% hematocrit, use of whole blood versus washed RBCs suspended in 10% dextran solution). However, due to more preparation steps, the potential for damage accumulation in multi-pass experiments, and the loss of the protective effect of plasma (Kameneva et al. 1997), we would expect that the washed RBCs used by Kameneva et al. (2004) may have been more fragile than the whole blood RBCs used by Ding et al. (2015). Thus, the significantly greater C coefficient obtained by Ding et al. (2015) is most likely due to device-specific differences in the flow conditions.

Finally, to highlight the importance of using device-specific power law coefficients, we compare hemolysis predictions in the capillary tube using the idealized global empirical coefficients of Ding et al. (2015) for bovine blood with the experimental data of Kameneva et al. (2004). We found that using traditional empirical coefficients yields a hemolysis prediction that is in error by more than 2000% compared to experiments. That is, even for the relatively simple flow conditions present in a capillary tube, using idealized power law coefficients from uniform shear experiments leads to extremely poor hemolysis predictions. It is no wonder that it is challenging to accurately predict absolute hemolysis levels in medical devices with complex flow conditions using the traditional approach (Fig. 1a).

Our CFD-based Kriging surrogate modeling framework that we present here is a powerful practical tool for determining device- and species-specific hemolysis power law coefficients for blood-contacting medical devices. In the near term, our approach may be used to assemble a database of empirical coefficients for the power law model for a range of devices and species of animal blood, which may then be used as a resources by others to characterize the hemolytic potential of their device. We believe that this approach (Fig. 1b) may be used in lieu of the traditional approach (Fig. 1a) to improve the predictive accuracy of the hemolysis power law model until more advanced physics-based models are developed. In the intermediate and long term, our CFD-based Kriging surrogate modeling framework may also be used to determine empirical coefficients that will undoubtedly exist in new and improved continuum-scale hemolysis models, and for models of other forms of flow-induced blood damage (e.g., platelet activation and thrombosis).

Acknowledgements The authors thank C. Paulson and P. Hariharan for helpful discussions. We also thank T. Zhang for clarifying the development of the power law coefficients for ovine blood that are provided in Table 1. Additionally, thanks to M. Myers and T. Morrison for reviewing the manuscript. This study used the computational resources of the high-performance computing clusters at the US Food and Drug Administration (FDA), Center for Devices and Radiological Health (CDRH). The findings and conclusions in this article have not been formally disseminated by the US FDA and should not be construed to represent any agency determination or policy. The mention of commercial products, their sources, or their use in connection with material reported herein is not to be construed as either an actual or implied endorsement of such products by the Department of Health and Human Services.

Compliance with ethical standards

Conflicts of interest The authors declare that they have no conflicts of interest.

Appendix 1: Hemolysis indices

In the approach presented here, we combine either analytical or numerical solutions of the Eulerian power law model with experimental data to determine device-specific hemolysis power law coefficients. A thorough understanding of the experiments is thus required—in particular, the way in which

the hemolysis data are measured and how this is replicated in the analytical or numerical approach. This in turn depends on the type of hemolysis experiment that is performed, of which there are two types: single-pass and multi-pass.

For a single-pass experiment, a given volume of blood passes through the device once over an elapsed period of time. The blood that passed through the device is then thoroughly mixed and a small volume (~ 1 ml) is sampled and centrifuged to separate the remaining red blood cells from the plasma and other blood elements. The concentration of plasma free hemoglobin, *fHb*, is then measured using spectrophotometry (Malinauskas 1997). Since *fHb* is measured in the absence of the remaining red blood cells, it has units of mass per volume of plasma (typically mg/dl). Given the total blood hemoglobin concentration (in units of mg/dl of whole blood), *Hb*, and the percent hematocrit, H_{ct}, the hemolytic potential of the device is typically quantified in terms of a single-pass index of hemolysis:

$$IH_{sp} = \frac{\left(1 - H_{ct}/100\right) fHb}{Hb}.$$

Physically, IH_{sp} represents the relative mass fraction of the total blood hemoglobin that is released from the RBCs as blood flows through the device. By definition, IH_{sp} must be between 0 and 1.

In multi-pass experiments, hemolysis measurements are typically performed with the medical device placed in a flow loop with recirculating whole blood (Fig. 8a). A small sample (~ 1 ml) of blood is drawn at incremental time points (e.g., every 30 min) and similarly centrifuged and assayed for *fHb* as described previously. Measurements of *fHb* are then plotted versus time, which typically yields a linear relationship (e.g., see Fig. 8b) as long as the release of plasma free hemoglobin is small compared to the total amount of hemoglobin—namely, if $\left(1 - H_{ct}/100\right) fHb \ll Hb$. Given *fHb*, *Hb*, and H_{ct}, the hemolytic potential of the device is often quantified in terms of a "modified index of hemolysis" (*MIH*) defined as

$$MIH = 10^6 \frac{\left(1 - H_{ct}/100\right) fHb}{Hb} \left(\frac{V}{Q\,\Delta t}\right)$$

where V is the total volume of blood in the flow loop, Q is the volumetric flow rate, and Δt is the time duration of the experiment (Mueller et al. 1993). The units of V, Q, and Δt are arbitrary as long as the quantity $(V/Q\,\Delta t)$ is dimensionless. The 10^6 scaling factor is introduced by convention to obtain quantitative values of reasonable magnitude.

Close inspection of the definition of *MIH* reveals that it effectively represents a scaled form of IH_{sp}, defined per pass through the multi-pass system and scaled by 10^6. This is evident by considering that $(Q\,\Delta t)$ is the total volume of blood pumped through the flow loop of volume V during the experiment. The term $(Q\,\Delta t)/V$ is thus the total effective number of passes that the blood has made through the flow loop. Accordingly, in dividing the right-hand side of *MIH* by $(Q\,\Delta t)/V$, the measurements of *fHb* are effectively normalized by the number of passes through the device. This is readily apparent if we consider an experiment in which all of the blood passes through the flow loop once (i.e., a single-pass), in which case $Q\,\Delta t = V$ and from the definitions of IH_{sp} and *MIH* we see that $MIH = 10^6 IH_{sp}$ in this case. Thus, in general, *MIH* physically represents the relative fraction of the total blood hemoglobin that is released from the RBCs per pass through the device. By definition, then, *MIH* must be between 0 and 10^6.

To directly compare with hemolysis experiments, an appropriate index of hemolysis must be calculated from analytical or numerical solutions of flow and hemolysis in

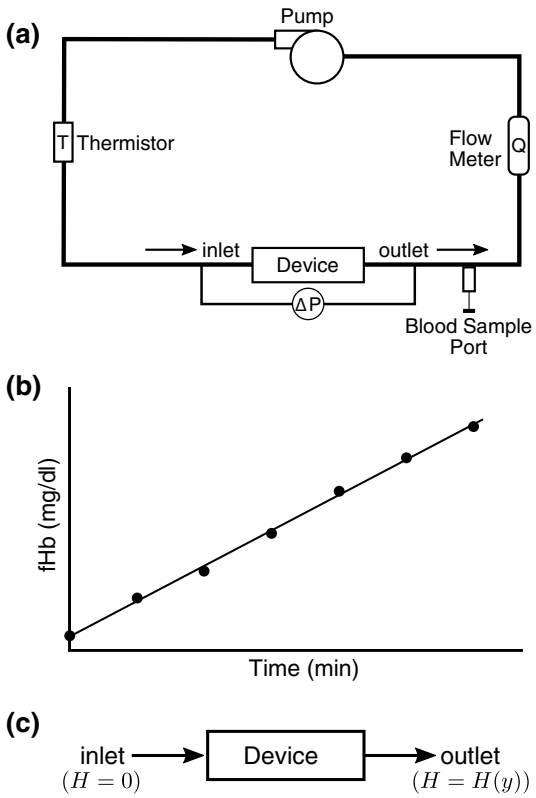

Fig. 8 Multi-pass experimental flow loop used for hemolysis testing versus the computational domain used for CFD simulations. **a** Schematic diagram of a typical flow loop used to acquire multi-pass experimental measurements of hemolysis generated by a medical device. **b** Notional plot of plasma free hemoglobin concentration (*fHb*) measured at various time points during experiments performed in the flow loop. The *fHb* versus time trend is generally linear for a well-controlled experiment as long as the release of plasma free hemoglobin is small compared to the total amount of hemoglobin—i.e., if $\left(1 - H_{ct}/100\right) fHb \ll Hb$. **c** Schematic diagram of a computational domain typically used in CFD simulations performed to predict the hemolytic potential of a medical device

a medical device. This is complicated by two factors. First, the physical domain represented in the analytical or computational model is generally not the same as the experimental domain. For example, the computational domain used for CFD is usually restricted to the device alone and does not include the entire flow loop (Fig. 8c). Second, analytical or numerical calculations are typically performed to predict device performance at steady state using a value of $H = 0$ at the inlet (Fig. 8c), as opposed to simulating the full hemolytic time history of the device (e.g., Fig. 8b).

Both of these complications are addressed by deriving an equivalent index of hemolysis that may be calculated from steady-state analytical or numerical solutions in any flow domain with an inlet and outlet. Considering a control volume containing only the device (Fig. 8c) and assuming an inlet value of $H = 0$, the production rate of H in the device at steady state may be calculated from conservation of mass as the integrated flux of H at the outlet—i.e., $\dot{H}_{\text{Device}} = \int_{\text{outlet}} (H\,\mathbf{u}) \cdot \mathrm{d}\mathbf{A}$, where $\mathrm{d}\mathbf{A}$ is the outlet area vector. If we normalize this by the integrated outlet flow rate ($\int_{\text{outlet}} \mathbf{u} \cdot \mathrm{d}\mathbf{A}$), we arrive at an expression that is equivalent to calculating the volume-weighted value of H at the outlet:

$$IH_{\text{outlet}} = \overline{H}_{\text{outlet}} = \frac{\int_{\text{outlet}} (H\,\mathbf{u}) \cdot \mathrm{d}\mathbf{A}}{\int_{\text{outlet}} \mathbf{u} \cdot \mathrm{d}\mathbf{A}}$$

which also represents an effective single-pass index of hemolysis that may be directly compared with experimental measurements. Akin to the "bulk temperature" used in the field of heat transfer (Bird et al. 2002), this single-pass definition of IH_{outlet} physically represents the index of hemolysis that would be measured if all of the blood having passed through the device were to be collected and well mixed. Accordingly, when comparing to single-pass measurements, IH_{outlet} is directly related to the experimental value of IH_{sp}. For multi-pass measurements, given that MIH represents a scaled form of IH_{sp} defined per pass of blood through the system, steady-state analytical or numerical predictions of IH_{outlet} for a multi-pass device may be scaled by 10^6 and directly compared with experimental values of MIH.

Appendix 2: Analysis of Kameneva et al. (2004) hemolysis data

Plasma free hemoglobin concentration: Using Plot Digitizer (http://plotdigitizer.sourceforge.net), the data in Table 2 were extracted from Fig. 6 of Kameneva et al. (2004) for the increase in plasma free hemoglobin concentration, fHb, from their laminar flow experiments.

Experimental parameters: Kameneva et al. (2004) report that the hematocrit (H_{ct}) of the red blood cell (RBC) suspension was 24.0%, the volume (V) of the flow loop was 250 ml, and the time duration of each experiment (Δt) was 90 min.

Table 2 Increase in plasma free hemoglobin concentration, fHb, extracted from Fig. 6 of Kameneva et al. (2004) for their laminar flow experiments. Here, fHb_{mean} is the mean experimental value, and fHb_{max} and fHb_{min} are the mean plus and minus one standard deviation (SD), respectively

Wall shear stress condition (Pa)	fHb_{min} (mg/dl)	fHb_{mean} (mg/dl)	fHb_{max} (mg/dl)
200	2.37	4.67	6.46
300	5.50	12.48	18.94
400	19.83	28.28	37.24

Flow rate: We also need the flow rate at each condition, which is not provided, to calculate the modified index of hemolysis (MIH). Kameneva et al. (2004) report that they measured the pressure drop, Δp, across the capillary tube and used the following simplified force balance to calculate the average wall shear stress, $\overline{\sigma}_{\text{wall}}$, at each condition:

$$\Delta p \pi R^2 = 2\pi R L \overline{\sigma}_{\text{wall}}$$

where R and L are the radius and length of the tube, respectively. Note that this expression neglects entrance effects in the developing flow region of the capillary tube and, therefore, implicitly assumes that the flow is fully developed. In theory, we could extend this fully developed flow relationship and calculate an estimate of the flow rate at each condition using the analytical circular Poiseuille flow solution for volumetric flow rate as a function of wall shear stress. However, the flow in the capillary tube of Kameneva et al. (2004) is not fully developed, especially at the higher flow rate conditions (see Sect. 4.3). Thus, any flow rate estimate calculated assuming fully developed flow would be incorrect. A more accurate approach is to use CFD to replicate the developing flow conditions present in the experiments. In this way, as described in Sect. 4.3, we used CFD to compute the laminar developing flow in the capillary tube at each condition ($\overline{\sigma}_{\text{wall}}$ of 200, 300, and 400 Pa). Given the CFD solution, we then calculate the volumetric flow rate, Q, by numerically integrating the velocity profile at the outlet (Table 3).

Table 3 Volumetric flow rate, Q, for laminar developing flow through the small capillary tube of Kameneva et al. (2004) computed by replicating the geometry and flow conditions using CFD for three operating conditions (see Sect. 4.3 for further details)

Wall shear stress condition (Pa)	Q (l/min)
200	0.148
300	0.207
400	0.259

Table 4 Modified index of hemolysis, *MIH*, calculated for the laminar experiments of Kameneva et al. (2004). Here, MIH_{mean} is the mean experimental value, and MIH_{max} and MIH_{min} are the mean plus and minus one SD, respectively

Wall shear stress condition (Pa)	MIH_{min}	MIH_{mean}	MIH_{max}
200	4.21	8.31	11.49
300	7.03	15.94	24.20
400	20.23	28.84	37.98

Total blood hemoglobin concentration: The total blood hemoglobin concentration, *Hb*, is not provided by Kameneva et al. (2004), but can be estimated. Given the reported hematocrit, we use the following relationship of Briggs and Bain (2017) to calculate an estimate of the total blood hemoglobin concentration, *Hb*:

$$Hb\,(\mathrm{g/dl}) = \frac{H_{ct}\,(\%)}{3}.$$

Accordingly, for the Kameneva et al. (2004) experiments where $H_{ct} = 24.0\%$, we calculate $Hb = 8$ g/dl $= 8000$ mg/dl.

Modified index of hemolysis (MIH): Finally, using Eq. 10, we calculate the values of *MIH* (Table 4) for the laminar experiments of Kameneva et al. (2004).

Appendix 3: Verification of CFD-based Kriging surrogate modeling

To verify our CFD-based Kriging surrogate modeling framework presented in Sect. 3.6 and to determine the best surrogate modeling strategy, we consider circular Poiseuille flow and compare with the analytical solution presented in Sect. 4.2. Due to the smooth nature of the hemolysis solution in (C, a, b) parameter space (see Fig. 6a), we found that accurately predicting the global response function using Kriging surrogate modeling is not especially challenging provided that several technical details are properly addressed. To increase the predictive accuracy of the surrogate model in the domain of interest, we restrict the parameter space domain to broadly encompass the range of values reported in the literature (Table 1) and the range of device-specific values observed in the analytical analyses for planar Couette flow (Sect. 4.1) and circular Poiseuille flow (Sect. 4.2). In particular, the power law coefficient C is restricted to be between 10^{-11} and 10^{-5}, the coefficient a to be between 0.1 and 1, and b is restricted to be between 0.5 and 4. We note that in choosing the parameter space range for the a coefficient, we also took into consideration the fact that there are biophysical reasons for why a should in theory be less than unity (see Yu et al. 2017). Additionally, we chose a lower limit of 0.1 for a to avoid numerical instabilities that develop as the Eulerian power law model source term (the right-hand side of Eq. 5), which is raised to the power of $1/a$, becomes unbounded as a approaches 0.

In applying the Kriging surrogate modeling framework, we also found that both the C coefficient and the hemolysis response field values need to be log10-transformed to obtain an accurate surrogate model. This is because the range of the C coefficient spans many orders of magnitude (a much wider range compared to the a and b coefficients) as do the values of *MIH* (see Fig. 6a). Accordingly, in preliminary analyses we found that log10-transformation of both the C coefficient and *MIH* field values from CFD is required in the Kriging interpolation step of the analysis to obtain a surrogate model that accurately represents the global hemolysis response function.

As shown in Algorithm 2, there are several input parameters in the Kriging surrogate modeling framework that need to be specified. By comparing with the analytical solution for circular Poiseuille flow, we can tune these parameters to obtain a globally accurate surrogate model of the hemolysis response function. The four main input parameters that need to be specified include the parameter space discretization level, the number of initial sample points, the number of infill points per iteration, and the convergence criterion of the algorithm. Because we seek a globally accurate surrogate model, we generate infill points using the root mean squared error (RMSE) criterion of the hemolysis response function obtained from the Kriging predictor (see Sect. 3.6).

In performing Kriging surrogate modeling for circular Poiseuille flow with $\sigma_{wall} = 400$ Pa using different levels of (C, a, b) parameter space discretization (100^3, 200^3, 300^3), we found that the predicted *MIH* field and various extracted isosurfaces were indistinguishable between the three cases. Thus, in all subsequent analyses we use a uniform parameter space discretization of 100^3 (i.e., $100 \times 100 \times 100$) to obtain a high-fidelity representation of the hemolysis response function. Additionally, by performing a parametric study using different numbers of initial sample points and infill points we found that we could obtain a globally accurate surrogate model using a set of 40 initial data points with no additional infill iterations. While additional infill iterations using the RMSE criterion were beneficial when fewer than 40 initial data points were used, there was little benefit (in terms of the predicted maximum normalized RMSE and in the accuracy of the predicted *MIH* field) when infill iterations were used with a Kriging predictor initialized with 40 or more data points. In this way, with a total of 40 CFD simulations (40 initial, no infill) we were able to obtain a globally accurate representation of the hemolysis response field with a predicted maximum normalized RMSE of less than 0.1%.

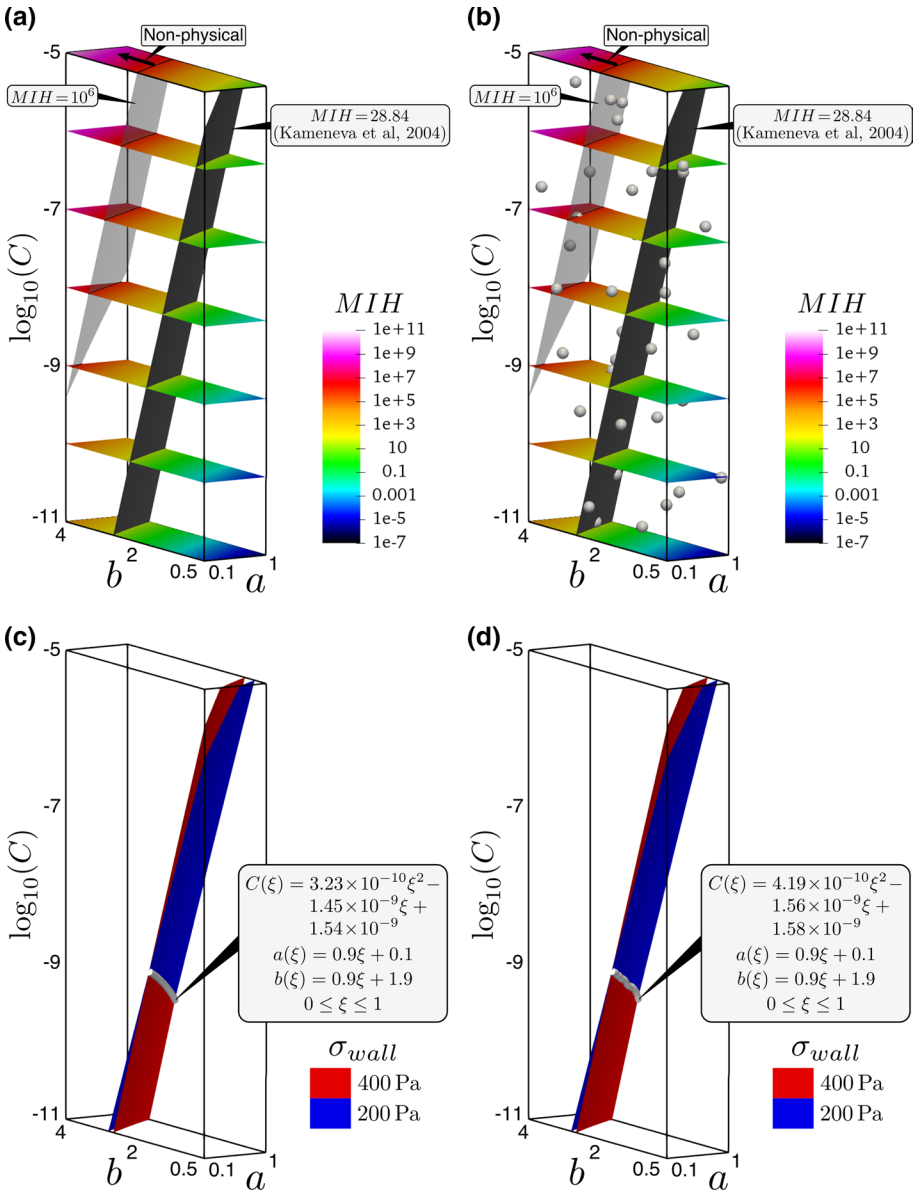

Fig. 9 Verification of CFD-based Kriging surrogate modeling for predicting device- and species-specific hemolysis power law coefficients for circular Poiseuille flow. **a** Analytical map of the modified index of hemolysis, *MIH*, in (C, a, b) parameter space for a single operating condition ($\sigma_{\text{wall}} = 400$ Pa). **b** Numerical map of the *MIH* response field for $\sigma_{\text{wall}} = 400$ Pa obtained using CFD and Kriging surrogate modeling. The 40 CFD sample points used to construct the surrogate model are also shown. In both panels a and b, an isosurface of $MIH = 28.84$ is shown, which corresponds to the mean experimental data of Kameneva et al. (2004) from hemolysis measurements in a small capillary tube with $\overline{\sigma}_{\text{wall}} = 400$ Pa using a suspension of bovine red blood cells. An isosurface of $MIH = 10^6$ is also shown in both panels as the delineation between physical ($MIH \le 10^6$) and non-physical ($MIH > 10^6$) hemolysis solutions. **c** Line of intersection obtained by performing a Boolean intersection of the isosurfaces of *MIH* extracted from the analytical hemolysis response field corresponding to the mean experimental measurements of Kameneva et al. (2004) at two operating conditions ($\overline{\sigma}_{\text{wall}}$ of 200 and 400 Pa). A parametric curve fit of the 200–400 Pa line of intersection obtained from the analytical solution yields: $C(\xi) = 3.23\times10^{-10}\xi^2 - 1.45\times10^{-9}\xi + 1.54\times10^{-9}$, $a(\xi) = 0.9\xi + 0.1$, and $b(\xi) = 0.9\xi + 1.9$, where ξ is the parametric variable defined as $0 \le \xi \le 1$. **d** 200–400 Pa line of intersection obtained with the same approach as in **c**, but using numerical results from CFD and Kriging surrogate modeling. A parametric curve fit of the 200–400 Pa line of intersection obtained using CFD-based Kriging surrogate modeling yields: $C(\xi) = 4.19\times10^{-10}\xi^2 - 1.56\times10^{-9}\xi + 1.58\times10^{-9}$, $a(\xi) = 0.9\xi + 0.1$, and $b(\xi) = 0.9\xi + 1.9$

Comparing Kriging surrogate model predictions with the analytical solution for circular Poiseuille flow (Sect. 4.2), the results are in close agreement. As shown in Fig. 9a and 9b, the global variation in the surrogate model prediction of the *MIH* response field for the condition with $\sigma_{\text{wall}} = 400$ Pa is indistinguishable from the analytical solution. To quantitatively verify the use of CFD-based Kriging surrogate modeling for determining device-specific hemolysis power law coefficients, we also computed surrogate model predictions for circular Poiseuille flow with a σ_{wall} of 200 and 300 Pa. We then extracted isosurfaces corresponding to the hemolysis measurements of Kameneva et al. (2004) at each condition, performed a Boolean intersection of each of the isosurfaces, and extracted the lines of intersection that are used to determine the device-specific coefficients (see Sect. 4.2). As shown in Fig. 9c, d, using Kriging surrogate modeling we obtain a 200–400 Pa line of intersection that closely matches that obtained with the analytical solution. The parametric curve fit of the 200–400 Pa line of intersection is extremely similar in each case, with the same parametric equation for $a(\xi)$ and $b(\xi)$ obtained from analytical and surrogate modeling approaches, where ξ is the parametric variable defined as $0 \le \xi \le 1$. There are relatively small differences between the analytical and numerical results for $C(\xi)$ that range from 1–3% at small values of ξ to less than 7% at large values of ξ. Importantly, however, these differences in $C(\xi)$ are small compared with the reported uncertainty in the hemolysis measurements of Kameneva et al. (2004). That is, as shown in Sect. 4.2 using the analytical solution, the 200–400 Pa line of intersection obtained using Kriging surrogate modeling falls within the small envelope in (C, a, b) parameter space that encompasses hemolysis values corresponding to the uncertainty bounds of the experimental data at all three conditions considered (σ_{wall} of 200, 300, and 400 Pa; see Sect. 4.2 for further discussion). Thus, in application such small differences in the analytical versus numerical $C(\xi)$ yield insignificant differences in the prediction of *MIH* compared with the uncertainty in the measurements.

In summary, given the close correspondence between the analytical and numerical results, this verifies the use of our CFD-based Kriging surrogate modeling approach for predicting device-specific hemolysis power law coefficients. In this case, 40 CFD simulations were used to predict the hemolysis response field at each operating condition, requiring a total of 120 CFD simulations for all three conditions. If only the extreme conditions (σ_{wall} of 200 and 400 Pa) are considered to extract the 200–400 Pa line of intersection that is used to determine the device-specific coefficients, this is reduced to a total of 80 CFD simulations. Fewer CFD simulations could potentially be used, albeit at the cost of a reduction in accuracy of the surrogate model predictions and the resultant device-specific coefficients.

Appendix 4: Capillary tube CFD mesh refinement study

To ensure that the CFD results of flow and hemolysis in the capillary tube of Kameneva et al. (2004) are insensitive to the mesh resolution, we performed a mesh refinement study comparing CFD predictions at the highest flow rate condition ($\overline{\sigma}_{\text{wall}} = 400$ Pa) using two meshes. Both meshes have a relatively high spatial resolution to resolve the plasma free hemoglobin boundary layer that is confined close to the wall when using some combinations of power law coefficients (e.g., small values of a and large values of b). The axisymmetric medium mesh (Fig. 10b) contains approximately 139,000 computational cells. The fine mesh (Fig. 10c) was generated by refining the medium mesh by a factor of $\sqrt{2}$, which resulted in slightly more than twice the number of computational cells (approximately 284,000). Steady-state CFD simulations of the flow showed a mere 0.0031% difference in the induced flow rate through the capillary tube using the same prescribed inlet–outlet pressure difference of 112 kPa (Table 5). Three different hemolysis simulations were performed for each mesh using different combinations of power law coefficients that span the parameter space range of interest. The results showed that the predicted values of *MIH* using the medium and fine meshes differ by between 0.033 and 3.4%, depending on the combination of power law coefficients (see Table 5). The largest difference was obtained using the smallest value of the a coefficient, which is due to the need to resolve the large streamwise flux associated with the extremely thin plasma free hemoglobin boundary layer that develops on the wall when small values of a and large values of b are used in the Eulerian power law model. Even so, such small differences between the medium and fine meshes demonstrate that the flow and hemolysis predictions are fairly insensitive to further refinement at this level of mesh resolution. Thus, the fine CFD mesh was used to predict the device- and species-specific hemolysis power law coefficients.

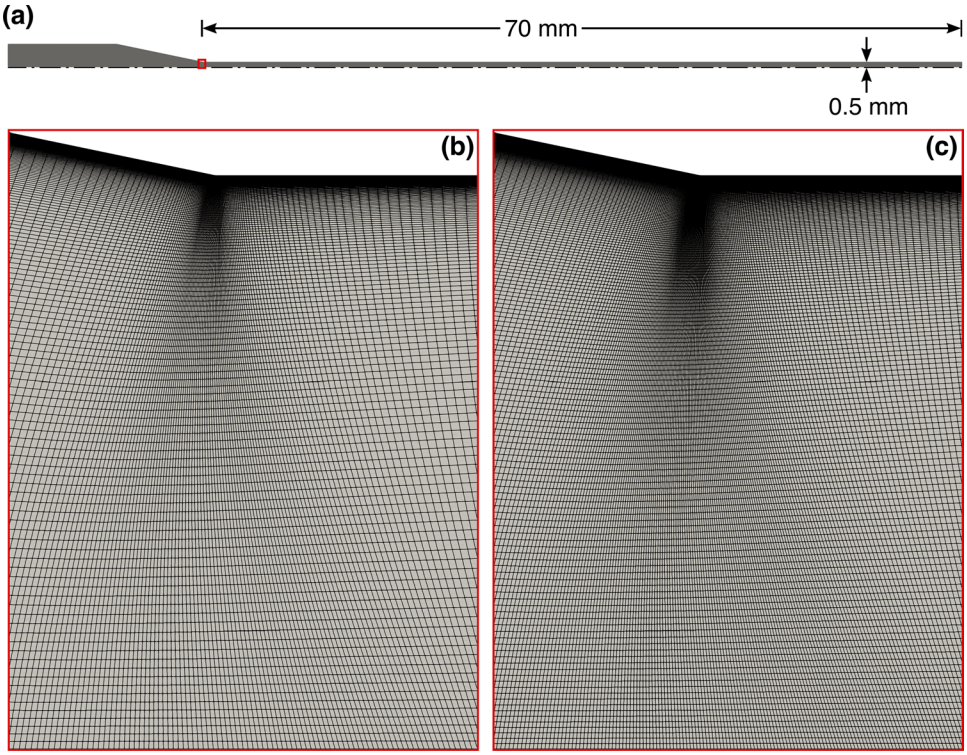

Fig. 10 Capillary tube geometry and CFD mesh. **a** Axisymmetric CFD model of the capillary tube of Kameneva et al. (2004). **b**, **c** Enlarged view of the inset region in panel a showing the **b** medium and **c** fine CFD meshes that contain approximately 139,000 and 284,000 computational cells, respectively. Note that a high spatial resolution was used to resolve the plasma free hemoglobin boundary layer that is confined close to the wall with some combinations of power law coefficients (e.g., small values of a and large values of b)

Table 5 Results of the capillary tube CFD mesh refinement study at the highest flow rate condition ($\overline{\sigma}_{\text{wall}} = 400$ Pa)

Quantity	Medium mesh	Fine mesh	% Diff.
Q (l/min)	0.25872778	0.25871975	0.0031
MIH 1	2675.908	2771.110	3.4
MIH 2	15561.564	15578.525	0.11
MIH 3	12692.403	12696.544	0.033

Q is the volumetric flow rate through the capillary tube. *MIH* 1 corresponds to the case with power law coefficients of $C = 1 \times 10^{-7}, a = 0.1$, and $b = 2$; *MIH* 2 corresponds to the case with $C = 1 \times 10^{-8}, a = 0.4$, and $b = 3$; and *MIH* 3 corresponds to the case with $C = 1 \times 10^{-10}, a = 0.7$, and $b = 4$

References

Alemu Y, Bluestein D (2007) Flow-induced platelet activation and damage accumulation in a mechanical heart valve: numerical studies. Artif Organs 31(9):677–688. https://doi.org/10.1111/j.1525-1594.2007.00446.x

Apel J, Paul R, Klaus S, Siess T, Reul H (2001) Assessment of hemolysis related quantities in a microaxial blood pump by computational fluid dynamics. Artif Organs 25(5):341–347

Arora D, Behr M, Pasquali M (2004) A tensor-based measure for estimating blood damage. Artif Organs 28(11):1002–1015

Aycock KI, Campbell RL, Lynch FC, Manning KB, Craven BA (2016) The importance of hemorheology and patient anatomy on the hemodynamics in the inferior vena cava. Ann Biomed Eng 44(12):3568–3582

Bird RB, Stewart WE, Lightfoot EN (2002) Transport phenomena, 2nd edn. Wiley, New York

Blackshear PL Jr, Dorman FD, Steinbach JH (1965) Some mechanical effects that influence hemolysis. ASAIO J 11(1):112–117

Blackshear P Jr, Dorman F, Steinbach J, Maybach E, Singh A, Collingham R (1966) Shear, wall interaction and hemolysis. ASAIO J 12(1):113–120

Bludszuweit C (1995) Three-dimensional numerical prediction of stress loading of blood particles in a centrifugal pump. Artif Organs 19(7):590–596

Bodnár T (2014) On the Eulerian formulation of a stress induced platelet activation function. Math Biosci 257:91–95. https://doi.org/10.1016/j.mbs.2014.06.010

Briggs C, Bain BJ (2017) Dacie and Lewis practical haematology, chap 3: basic haematological techniques. 12th edn. Elsevier, London, pp 18–49

Chen Y, Sharp MK (2010) A strain-based flow-induced hemolysis prediction model calibrated by in vitro erythrocyte deformation measurements. Artif Organs 35(2):145–156

Ding J, Niu S, Chen Z, Zhang T, Griffith BP, Wu ZJ (2015) Shear-induced hemolysis: species differences. Artif Organs 39(9):795–802

Ezzeldin HM, de Tullio MD, Vanella M, Solares SD, Balaras E (2015) A strain-based model for mechanical hemolysis based on a coarse-grained red blood cell model. Ann Biomed Eng 43(6):1398–1409

Faghih MM, Sharp MK (2016) Extending the power-law hemolysis model to complex flows. J Biomech Eng 138(12):124504

Faghih MM, Sharp MK (2018) Characterization of erythrocyte membrane tension for hemolysis prediction in complex flows. Biomech Model Mechanobiol. https://doi.org/10.1007/s10237-017-0995-2

Forrester A, Sobester A, Keane A (2008) Engineering design via surrogate modelling: a practical guide. Wiley, New York

Fraser KH, Zhang T, Ertan Taskin M, Griffith BP, Wu ZJ (2012) A quantitative comparison of mechanical blood damage parameters in rotary ventricular assist devices: shear stress, exposure time and hemolysis index. J Biomech Eng 134(8):081002

Garon A, Farinas MI (2004) Fast three-dimensional numerical hemolysis approximation. Artif Organs 28(11):1016–1025
Giersiepen M, Wurzinger L, Opitz R, Reul H (1990) Estimation of shear stress-related blood damage in heart valve prostheses-in vitro comparison of 25 aortic valves. Int J Artif Organs 13(5):300–306
Goubergrits L, Affeld K (2004) Numerical estimation of blood damage in artificial organs. Artif Organs 28(5):499–507
Goubergrits L, Osman J, Mevert R, Kertzscher U, Pöthkow K, Hege HC (2016) Turbulence in blood damage modeling. Int J Artif Organs 39(4):160–165. https://doi.org/10.5301/ijao.5000476
Grigioni M, Daniele C, Morbiducci U, D'Avenio G, Di Benedetto G, Barbaro V (2004) The power-law mathematical model for blood damage prediction: analytical developments and physical inconsistencies. Artif Organs 28(5):467–475
Grigioni M, Morbiducci U, D'Avenio G, Benedetto GD, Gaudio CD (2005) A novel formulation for blood trauma prediction by a modified power-law mathematical model. Biomech Model Mechanobiol 4(4):249–260. https://doi.org/10.1007/s10237-005-0005-y
Hariharan P, D'Souza G, Horner M, Malinauskas R, Myers M (2015) Verification benchmarks to assess the implementation of computational fluid dynamics based hemolysis prediction models. J Biomech Eng 137:094501
Hariharan P, Aycock KI, Buesen M, Day SW, Good BC, Herbertson LH, Steinseifer U, Manning KB, Craven BA, Malinauskas RA (2018) Inter-laboratory characterization of the velocity field in the FDA blood pump model using particle image velocimetry (PIV). Cardiovasc Eng Technol 9:623–640. https://doi.org/10.1007/s13239-018-00378-y
Heck ML, Yen A, Snyder TA, O'Rear EA, Papavassiliou DV (2017) Flow-field simulations and hemolysis estimates for the Food and Drug Administration critical path initiative centrifugal blood pump. Artif Organs 41(10):E129–E140. https://doi.org/10.1111/aor.12837
Heuser G, Opitz R (1980) A Couette viscometer for short time shearing of blood. Biorheology 17(1–2):17–24
Jones DR (2001) A taxonomy of global optimization methods based on response surfaces. J Glob Optim 21(4):345–383
Kameneva MV, Antaki JF, Yeleswarapu KK, Watach MJ, Griffith BP, Borovetz HS (1997) Plasma protective effect on red blood cells exposed to mechanical stress. ASAIO J 43(5):M571–575
Kameneva MV, Burgreen GW, Kono K, Repko B, Antaki JF, Umezu M (2004) Effects of turbulent stresses upon mechanical hemolysis: experimental and computational analysis. ASAIO J 50(5):418–423
Kusserow B, Kendall L (1963) In vitro changes in the corpuscular elements of blood flowing in tubular conduits. ASAIO J 9(1):262–268
Malinauskas RA (1997) Plasma hemoglobin measurement techniques for the in vitro evaluation of blood damage caused by medical devices. Artif Organs 21(12):1255–1267
Malinauskas RA, Hariharan P, Day SW, Herbertson LH, Buesen M, Steinseifer U, Aycock KI, Good BC, Deutsch S, Manning KB, Craven BA (2017) FDA benchmark medical device flow models for CFD validation. ASAIO J 63(2):150–160
McKay MD, Beckman RJ, Conover WJ (1979) A comparison of three methods for selecting values of input variables in the analysis of output from a computer code. Technometrics 21(2):239–245
Mueller M, Schima H, Engelhardt H, Salat A, Olsen D, Losert U, Wolner E (1993) In vitro hematological testing of rotary blood pumps: remarks on standardization and data interpretation. Artif Organs 17(2):103–110
Paulson C, Ragkousis G (2015) pyKriging: a python Kriging toolkit. https://doi.org/10.5281/zenodo.21389
Pinotti M, Rosa ES (1995) Computational prediction of hemolysis in a centrifugal ventricular assist device. Artif Organs 19(3):267–273
Sohrabi S, Liu Y (2017) A cellular model of shear-induced hemolysis. Artif Organs 41(9):E80–E91. https://doi.org/10.1111/aor.12832
Song X, Throckmorton AL, Wood HG, Antaki JF, Olsen DB (2003) Computational fluid dynamics prediction of blood damage in a centrifugal pump. Artif Organs 27(10):938–941
Taskin ME, Fraser KH, Zhang T, Wu C, Griffith BP, Wu ZJ (2012) Evaluation of Eulerian and Lagrangian models for hemolysis estimation. ASAIO J 58(4):363–372
Taylor JO, Meyer RS, Deutsch S, Manning KB (2016) Development of a computational model for macroscopic predictions of device-induced thrombosis. Biomech Model Mechanobiol 15(6):1713–1731
Toninato R, Fadda G, Susin FM (2017) A red blood cell model to estimate the hemolysis fingerprint of cardiovascular devices. Artif Organs. https://doi.org/10.1111/aor.12937
Trias M, Arbona A, Masso J, Minano B, Bona C (2014) FDA's nozzle numerical simulation challenge: non-Newtonian fluid effects and blood damage. PLoS ONE 9(3):e92638
Vitale F, Nam J, Turchetti L, Behr M, Raphael R, Annesini MC, Pasquali M (2014) A multiscale, biophysical model of flow-induced red blood cell damage. AIChE J 60(4):1509–1516
White FM (2011) Fluid mechanics, 7th edn. McGraw-Hill, New York
Yu H, Engel S, Janiga G, Thévenin D (2017) A review of hemolysis prediction models for computational fluid dynamics. Artif Organs 41(7):603–621. https://doi.org/10.1111/aor.12871
Zhang T, Taskin ME, Fang HB, Pampori A, Jarvik R, Griffith BP, Wu ZJ (2011) Study of flow-induced hemolysis using novel Couette-type blood-shearing devices. Artif Organs 35(12):1180–1186